

CJSJ

*Columbia Junior
Science Journal*

2018-2019

Table of Contents

The Effects of Resveratrol and Nicotinamide Riboside on the Lifespan of Drosophila melanogaster	1	Ultrasensitive Volumetric Imaging Through Optical Coherence Tomography	19
By Jake Azrolan		By Ethan McFarlin	
Catecholamine Inhibition of IL-4 Induced B-Cell Activation	3	Ultrasensitive Volumetric Imaging Through Optical Coherence Tomography	21
By Ross Bernstein		By Riya Patel	
Analyzing the Effects of FXR and SP-C on Macrophage Inflammatory Response to Nitrogen Mustard and Ozone	5	Stabilization Of Amorphous Ddt In Polymers To Increase Lethality	23
By Catherine Buren		By Ethan Reiter	
A Taxonomic Morphometric Analyses between Extinct Dominican Amber Fossilized Formicidae from the Miocene and Extant Dominican Formicidae	7	Quitpuff: A Simple, Home-Based, Salivary Diagnostic Test to Assess Risk Of Oral Pre-Cancer And Cancer In Chronic Smokers	25
By Alan Chen		By Nikhiya Shamsher	
Change in Drosophila Receptor Activity and Contraceptive Pill Efficiency Due to Antibiotics	9		
By Emily Choe			
Facile Synthesis, Characterization and Electrochemical Testing of Lithium-ion battery cathode material	11		
By Vasu Kaker			
Fractal Analysis of Enzyme Active Site	13		
By Min Jae Kim			
A Customized Machine Learning Pipeline to Build State-of-the-Art Audio Classifiers	15		
By Sruthi Kurada			
A Rule-Based Natural Language Processing Pipeline for Anesthesia Classification From Unstructured Operative Notes	17		
By Mrunali Manjrekar			

CUSJ Board	Faculty Advisory Board
Micah Gay , President	Hugh Ducklow (Primary Advisor), Earth & Environmental Sciences
Christina Monnen , Managing Editor, CUSJ	Ivana Hughes , Chemistry
Anastasia Dmitrienko , Managing Editor, CJSJ	Marko Jovanovic , Biology
Alex Maddon , Director of Communications	Laura Kaufman , Chemistry
Ethan Chen , Director of Finance	Patricia Lindemann , Psychology
Jason Mohabir , Director of Events	Kyle Mandli , Applied Physics & Applied Math
Maya Talukdar , Director of Internal Affairs	Matthew Palmer , Ecology, Evolution & Environmental Biology
	Gerard Parkin , Chemistry
	Ron Prywes , Biological Sciences
	Angela Rasmussen , Mailman School of Public Health

The Effects of Resveratrol and Nicotinamide Riboside on the Lifespan of *Drosophila melanogaster*

Jake Azrolan

Abstract — Resveratrol (RSV) is a widely marketed longevity supplement that is a naturally occurring polyphenolic compound found in many fruits including grapes, peanuts, and berries [2]. The mechanism of action of RSV is dependent on the presence of a surplus of NAD⁺. Therefore, it is unclear how RSV might aid in longevity if not supplemented with NAD⁺. *Drosophila melanogaster* wild type were exposed to RSV and Nicotinamide Riboside (NR), a precursor to NAD⁺, either independently or in combination (RSV+NR) and compared to the control group.

I. INTRODUCTION

Modern trends in health science in popular culture involve widespread interest in supplements that can aid in longevity [9]. One supplement that is widely marketed as effective in this regard is Resveratrol. RSV, 3,5,4'-Trihydroxystilbene, works by activating the Sirtuin pathway, a molecular pathway involving a number of genes commonly referred to as longevity genes [10]. Sirtuin (SIRT) genes code for the SIRT1 family of proteins that are responsible for biological functions and aging [2]. Sirtuins make up a seven member class of proteins that function predominantly as NAD dependent deacetylases and use NAD⁺ as a substrate to remove acetyl groups from histones, which allows for condensing of DNA [6]. Given that the mechanism of action for RSV and its effect on longevity involves the activation of the SIRT pathway, which requires NAD⁺, it is unclear how RSV alone will affect longevity without additional surplus of NAD⁺. Nicotinamide Riboside (NR) is a precursory compound of NAD⁺⁺ that is readily available for use in the laboratory setting [7]. Through the salvage molecular pathway, NR undergoes phosphorylation to produce Nicotinamide Mononucleotide (NMN) utilizing NR kinase; NMN is then converted into NAD⁺ by NMN Adenyltransferase [11]. As such, NR may be a secondary supplement, that when administered in combination with RSV, may produce a greater effect than administration of RSV alone. This study investigated the longevity producing effects of RSV and NR in the common fruit fly, *D. melanogaster*, when used individually and in combination. *D. Melanogaster* was an ideal organism because it is a well-studied and provides a highly tractable genetic model organism that is used frequently in longevity research. It is easily attainable, inexpensive and has a rapid life cycle [8]. It was hypothesized that RSV given in combination with NR will increase the lifespan of *D. melanogaster* more than either treatment given independently.

II. METHODS

To examine the effects of RSV and NR on the survival rate of *D. melanogaster*, parent generation (P) flies were obtained from Ward Biologic, all at the same age. To eliminate food

source as a possible confound, generation one (G1) and subsequent generation two (G2) experimental flies were bred and all were exposed to standard medium 24-blue and 20 ml of the respective treatment. Experimental groups were designated as follows: RSV, NR, RSV+NR, and a control, no-treatment (NT) group. Each generation was produced by mating 4 groups of 15 males with 15 females for four days in an incubator set to 25°C. Adult G2 flies were transferred on the first day of adulthood (D1), using Flynap anesthesia, at a density of 30 flies per vial, in each of 4 vials – one for each experimental group. Mortality rates were recorded daily. Group differences for treatments were assessed using a one-way ANOVA, and survivorship curves were compared using a Kaplan-Meier approach. The Kaplan-Meier survival analysis is a powerful log-rank statistical test that is typically used to investigate questions involving survival rates within treatment groups. A chi-squared test statistic produced from this analysis indicates whether the survival rate for one group differs from any other groups with statistical significance [4].

III. RESULTS AND DISCUSSION

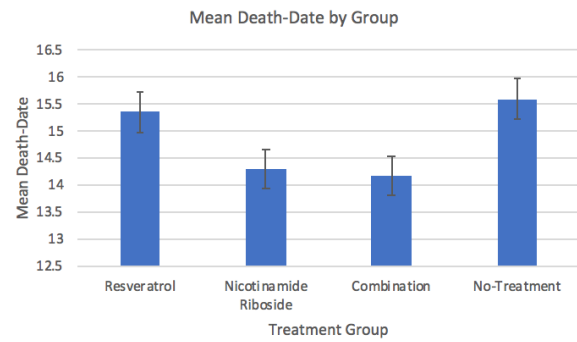


Figure 1: One-way ANOVA for test of group differences about the mean. Treatment did not have a significant effect on average lifespan ($F=0.32$, $p=0.812$), and NT flies, on average, survived the longest ($\mu=15.60$).

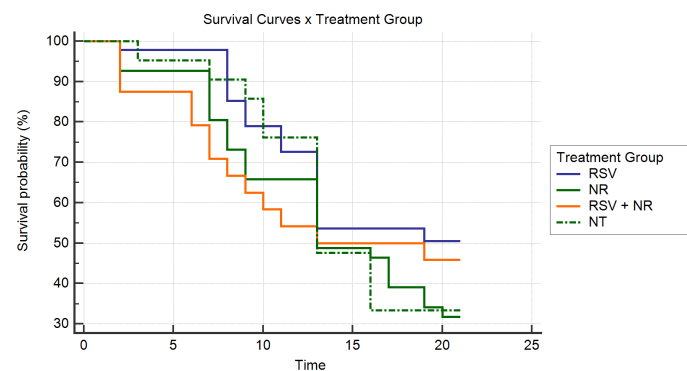


Figure 2: Kaplan-Meier Log-rank test for group differences in survival curves. Treatment group did not have a significant effect on mortality rate within the study period ($X^2=4.00$ $p=0.26$). A vertical gap between plotted curves indicates the greatest survivorship in the top-most curve, and a horizontal gap that it took longer for a given group to experience

On average, there was no significant difference between groups' average lifespans ($F=0.32$, $p=0.812$). Existing group differences are likely driven by a difference in average death-date in the No Treatment (NT) group ($\mu=15.60$) and the Resveratrol (RSV) group ($\mu=15.35$), from the two other groups, Nicotinamide Riboside (NR) ($\mu=14.16$ days) and RSV+NR ($\mu=14.29$ days). Flies in the NR and RSV+NR groups, on average, experienced shorter lifespans than flies in the other two groups. However, given that these results are not statistically significant, it is likely that any group differences were due to chance.

Survivor-curve analysis indicated that the risk of death is not consistently greater for one treatment group than another, but that there was a mild trend indicating a difference in survival probability between groups ($X^2=4.00$, $p=0.26$). Based on these results the survival rate was approximately equivalent in all groups. The results indicate that RSV and NR, two widely marketed products for improving longevity, are not effective in increasing lifespan. Consumers should be wary of claims that these supplements can have a marked effect on health. Given that Nicotinamide Riboside (NR) and Resveratrol (RSV) are contained in a variety of food sources, it will be of great interest to translate this study from this model organism, and examine whether these supplements can prevent age-associated physiological decline in humans. Limitations in the study design might limit interpretations to be drawn from this data as the average lifespan of *D. melanogaster* is longer than the current study period ($\mu \approx 50$ days) [5]. Further studies should be performed to investigate the efficacy of these treatments at different concentrations, and over a longer time period. Determination of a supplement capable of extending an organism's lifespan would revolutionize modern-day medicine.

IV. ACKNOWLEDGMENTS

I would like to thank Professor Joseph Dispigno and Dr. Allyson Weseley for this opportunity to conduct this research.

V. REFERENCES

- [1] Berman, A. Y., Motechin, R. A., Wiesenfeld, M. Y., & Holz, M. K. (2017). The therapeutic potential of resveratrol: a review of clinical trials. *NPJ precision oncology*, 1, 35.
- [2] Bhullar, K.S., & Hubbard, B.P. (2015). Lifespan and health spa extension by resveratrol. *Science Direct*, 1852(6), 1209-1218. Retrieved from <https://www.sciencedirect.com/science/article/pii/S0925443915000216>
- [3] Denu, J. (2007). Vitamins and Aging: Pathways to NAD + Synthesis. *Cell*. <https://doi.org/10.1016/j.ell.2007.04.023>
- [4] Goel, M., Khanna, P., & Kishore, J. (2011). Understanding survival analysis: Kaplan-Meier estimate. *International Journal of Ayurveda Research*. <http://doi.org/10.4103/0974-7788.7679>
- [5] Linford, N. J., Bilgir, C., Ro, J., & Pletcher, S. D. (2013). Measurement of Lifespan in *Drosophila melanogaster*. *Journal of Visualized Experiments*, (71). doi:10.3791/50068
- [6] Massudi H, Grant R, Braidy N, Guest J, Farnsworth B, Guillemin G. (2012). Age-Associated Changes In Oxidative Stress and NAD+ Metabolism In Human Tissue. *PlosOne* 7(7);e42357
- [7] Mills, K. F., Yoshida, S., Stein, L. R., Grozio, A., Kubota, S., Sasaki, Y., . . . Imai, S. (2016). Long-Term Administration of Nicotinamide Mononucleotide Mitigates Age-Associated Physiological Decline in Mice. *Cell Metabolism*, 24(6), 795-806. doi:10.1016/j.cmet.2016.09.013
- [8] Pandey, U. B., & Nichols, C. D. (2011). Human Disease Models in *Drosophila melanogaster* and the Role of the Fly in Therapeutic Drug Discovery. *Pharmacological Reviews*. 2 <https://doi.org/10.1124/pr.110.003293>
- [9] Timmers, S., Auwerx, J., & Schrauwen, P. (2012). The journey of resveratrol form yeast to human. *Impact Journals*, 4(3), 146-158. Retrieved from <https://www.ncbi.nlm.nih.gov/pmc/articles/PMC348475/>
- [10] Wood, J.G., Roglina, B., Lavu, S., Howard, K., Helfand, S.L., M., & Sinclair, D. (2004). Sirtuin activators mimic caloric restrictions and delay aging in metazoans. *Pubmed*, 4(18), 1-5. Retrieved from <https://www.ncbi.nlm.nih.gov/pubmed/15254550>
- [11] Yang, Y., & Sauve, A. A. (2016). NAD+ metabolism: Bioenergetics, signaling and manipulation for therapy. *Biochimica et Biophysica Acta - Proteins and Proteomics*. <http://doi.org/10.1016/j.bbapap.2016.06.014>

Catecholamine Inhibition of IL-4 Induced B-Cell Activation

Ross Bernstein

Abstract — Though seemingly separate, the nervous system plays a major part in modulation of the immune system. The Vagus Nerve transmits signals throughout the human body to control essential bodily functions. A branch of the Vagus Nerve innervates the spleen, where acetylcholine, adrenaline, and noradrenaline modulate TNF α release, by targeting T-cells and macrophages. However, it has not been investigated how the release of these neurotransmitters affect B-cells, immune cells that secrete antibodies (IgG). B-cells and T-cells were isolated from WT-Black 6 mice and treated with varying neurotransmitters to compare the effects. After treatment, the cells were stained and examined through flow cytometry to compare the percentage of T-cells, B-cells, and activated B-cells present in the population of lymphocytes. Our analysis indicated that epinephrine and norepinephrine increased B-cell activation, but more surprisingly they inhibited B-cell activation by IL-4.

I. INTRODUCTION

Inflammation is present in all diseases and is part of the natural human immune response. It can range from slight swelling to rampant systemic abnormalities¹, known as sepsis. Over 30 million patients per year are diagnosed with sepsis, and it is fatal for 20% of that population². Research into this possibly fatal disease could have multiple advantageous ramifications. Dr. Kevin Tracey and his laboratory defined the immune reflex³, and since its discovery, Dr. Tracey has spearheaded the development of an implantable stimulator on the Vagus Nerve. While this device has treated multiple immune diseases, it is not suited for emergency use, which is where sepsis causes the most harm. Other studies have investigated B-cell activation by lipopolysaccharide and concanavalin A⁺ and the effects of catecholamines on the activation of B-cells. These findings suggested an augmented inhibitory response by the catecholamines when compared to the other agonists, however the catecholamines inhibited a non-human activator, β -AR receptors, receptors for norepinephrine and epinephrine, are known to influence B-cell and T-cell activation, however the relationship between these receptors and immunocyte activation has not been investigated in the spleen. Our study aims to bridge those gaps by investigating the effects of various neurotransmitters on immune cell activation and differentiation. The findings of this study are preliminary to clinical applications, however, there are some viable applications, such as a treatment for an overproduction of antibodies in an emergent situation as a short-term treatment. Excitatory neurotransmitters are expected to cause the greatest change in IgG secretion levels.

II. METHODS

Spleens from Wildtype Black 6 mice were provided, and the splenocytes were isolated from RBCs and other cells. The cells were cultured in a media solution (See Appendix A). The cells were either plated directly or left to incubate for two days. After a two-day incubation period at 5% CO₂ and 37°C, the B-cells and T-cells were separated from the macrophages and monocytes. Cells were then plated in a 96-well plate at 2 X 10⁴ cells per well. The cells were treated with concanavalin

A (10 μ g/mL), acetylcholine (100 μ g/mL), histamine (100 μ g/mL), sodium valproate (100 μ g/mL), serotonin (100 μ g/mL), epinephrine (1 or 10 μ M) +/- IL-4 (10ng/mL), or norepinephrine (1 or 10 μ M) +/- IL-4. Each treatment had a column on the plate, in addition to an untreated column. The plates were then incubated for two days. After treatment, the supernatants were removed. The cells were treated with 150 μ L of 2mM EDTA and 2% FBS in HBSS to remove them from the wells. Then the cells were re-suspended in 50 μ L of 1% BSA in PBS and collected in 2 mL microcentrifuge tubes. The cells were stained for CD3 (T-cells), CD19 (B-cells), F480 (Macrophages), MHC II, CD11c (Monocytes), and CD169 (Activated B-cells) (Stains can be found in Appendix B). 1 μ L of each stain was combined together, and 6 μ L of the stain solution was added to each sample, excluding the unstained control. The samples were analyzed on FlowJo, a flow cytometry analysis software. The graphs (See Appendix B) only depicted single lymphocytes. Any aggregated cells were excluded. CD3 expression was compared against CD19 and CD169 expression (only for epinephrine and norepinephrine trials).

III. RESULTS

Treatments	Treatment Concentration	+/- IL-4	CD 19++ %	CD 19+ %*
A. Unstained	---	-		.28%
B. Untreated	---	-	2.90%	63.3%
C.	---	+	9.26%	
D. Con A	10 μ g/mL	-		69.9%
E. Acetylcholine	100 μ M	-		65.0%
F. Histamine	100 μ M	-		61.4%
G. Sodium Valproate	100 μ M	-		65.2%
H. Serotonin	100 μ M	-		65.1%
I. Epinephrine	1 μ M	-	3.51%	
J.		+	4.98%	
K.	10 μ M	-	2.73%	
L.		+	5.39%	
M. Norepinephrine	1 μ M	-	1.01%	
N.		+	3.70%	
O.	10 μ M	-	2.92%	
P.				
Q.		+	4.85%	

Figure 1: Table of Neurotransmitter Treatments – Rows E-H were completed in the first experimentation cycle. Rows I-Q were completed in the second experimentation cycle. The raw data that this table is constructed from can be found in Appendix B. *First trials did not specify for CD 19++ and only compared total B-cell populations

IV. CONCLUSION

At the conclusion of the study, the results contradicted the original hypothesis, as excitatory neurotransmitters were not found to cause noticeable changes in IgG antibody production. It was also found that epinephrine and IL-4 have an agonist-antagonist relationship when focusing on B-cell activation and differentiation, which has been supported by:

- A. IL-4 caused a 219% increase in B-cell activation in untreated cells.
- B. Epinephrine 1 μ M compared to untreated cells showed a 21% increase in B-cell activation, while epinephrine 1 μ M+IL-4 compared to untreated cells+IL-4 demonstrated a 46% decrease in B-cell activation.
- C. Epinephrine 10 μ M compared to untreated cells showed a 5.9% decrease in B-cell activation, while epinephrine 10 μ M+IL-4 compared to untreated cells+IL-4 demonstrated a 42% decrease in B-cell activation.
- D. Norepinephrine 1 μ M compared to untreated cells showed a 65% decrease in B-cell activation, while norepinephrine 1 μ M+IL-4 compared to untreated cells+IL-4 demonstrated a 60% decrease in B-cell activation.
 - 1. Though there is a smaller decrease in B-cell activation, this statistic still demonstrates large decreases in B-cell activation when reading raw data.
- E. Norepinephrine 10 μ M compared to untreated cells showed a .69% increase in B-cell activation, while norepinephrine 10 μ M+IL-4 compared to untreated cells+IL-4 demonstrated a 47% decrease in B-cell activation.

V. DISCUSSION

At the conclusion of the experimentation process, it was found that epinephrine and norepinephrine caused an inhibition of murine splenic cell activation and differentiation by IL-4. Surprisingly, no other neurotransmitter caused a noticeable positive or negative change in IgG levels. These findings refute the original hypothesis as not all excitatory neurotransmitters demonstrated a modulation in IgG levels. A possible explanation for this inhibition is allosteric inhibition. Catecholamines could potentially change the IL-4 receptors on B-cells and T-cells. It is known that β_2 -AR receptors affect T-helper cell 1 and 2 differentiation. Therefore, there is a possibility for allosteric inhibition of IL-4 on B-cell receptors. These findings support Dr. Tracey's report of Vagus Nerve stimulation inhibiting TNF α production. Norepinephrine and epinephrine are vital aspects of the inflammatory reflex that is controlled by the Vagus Nerve. Therefore, the inhibition of IL-4, another cytokine, activation of B-cells follows the same principles of Dr. Tracey's studies.

VI. ACKNOWLEDGEMENTS

I would like to thank Dr. Aisling Tynan, Dr. Sangeeta Chavan, and Dr. Kevin Tracey for giving me the opportunity to conduct this research.

VII. REFERENCES

- [1] Singer M, Deutschman CS, Seymour CW. The Third International Consensus Definitions for Sepsis and Septic Shock (Sepsis-3). *JAMA Network*
- [2] Sepsis. World Health Organization. <http://www.who.int/news-room/fact-sheets/detail/sepsis>. Published April 19, 2018.
- [3] Tracey KJ. The Inflammatory Reflex. *Nature*;420(6917):853-859. https://www.researchgate.net/publication/10983143_The_inflammatory_reflex
- [4] Koopman Frieda A., Chavan Sangeeta S., et al. Vagus Nerve Stimulation Inhibits Cytokine Production and Attenuates Disease Severity in Rheumatoid Arthritis. *PNAS*. 113 (29) 8284-8289
- [5] Cook-Mills JM, Cohen RL, Perlman RL, Chambers DA. Inhibition of Lymphocyte Activation by Catecholamines: Evidence for a Non-Classic Mechanism of Catecholamine Action. *Immunology*. 119(5):544-549. <https://www.ncbi.nlm.nih.gov/pmc/articles/PMC1383781/pdf/immunology0070-0030.pdf>.
- [6] Scanzano A, Cosentino M. Adrenergic regulation of innate immunity: a review. *Frontiers in Pharmacology*. 2015;6. <https://www.ncbi.nlm.nih.gov/pmc/articles/PMC4534859/pdf/fphar-00171.pdf>

APPENDIX A- Cell Culture Media

The media solution used during the splenocyte procurement process and the incubation period is comprised of the following:

1. 1% Gibco Glutamax (glutamate supplement)
2. 1% Gibco HEPES (buffer)
3. 1% Gibco Non-Essential Amino Acids (amino acid supplement)
4. 1% Gibco Penicillin-Streptomycin (antibiotics)
5. .1% Gibco beta-mercaptoethanol (oxygen radical reducer)
6. 10% Fetal Bovine Serum (growth factor)
7. 85.9% Gibco RPMI Media

APPENDIX B- Flow Cytometry Raw Data

Note: All graphs show CD19 on the x-axis and CD3 on the y-axis. Stain names follow the indicated markers.

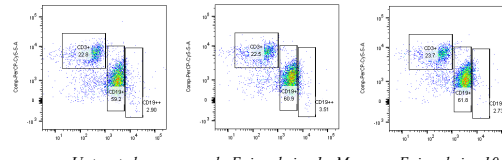


Figure B1: Flow Cytometry- Epinephrine - IL-4 - CD19 (BV786) v. CD3 (PerCP-Cy5.5)

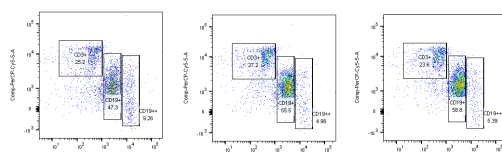


Figure B2: Flow Cytometry- Epinephrine + IL-4 - CD19 (BV786) v. CD3 (PerCP-Cy5.5)

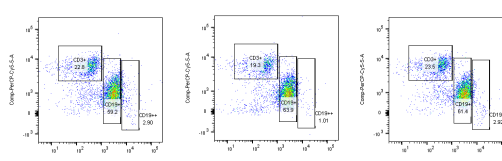


Figure B3: Flow Cytometry- Norepinephrine - IL-4 - CD19 (BV786) v. CD3 (PerCP-Cy5.5)

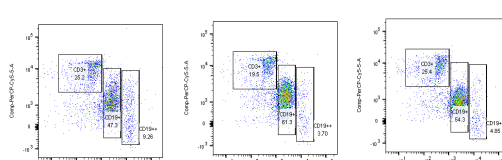


Figure B4: Flow Cytometry- Norepinephrine + IL-4 - CD19 (BV786) v. CD3 (PerCP-Cy5.5)

Analyzing the Effects of FXR and SP-C on Macrophage Inflammatory Response to Nitrogen Mustard and Ozone

Catherine E. Buren

Abstract — Nitrogen mustard (NM), a cytotoxic alkylating agent, and ozone, a highly reactive oxidant present in air pollution, contribute to pulmonary toxicity. Following NM or ozone exposure, there is a sequential accumulation of pro- inflammatory/cytotoxic and anti-inflammatory/wound repair macrophages in the lung, which have been implicated in disease pathogenesis. In these studies the effects of farnesoid x receptor (FXR) and surfactant protein c (SP-C) on macrophages accumulating in the lung were analyzed in response to NM and ozone, respectively. FXR is a nuclear receptor which downregulates inflammation. SP-C is essential for lung function and regulates inflammation. Increased quantities of iNOS pro-inflammatory macrophages in SP-C^{-/-} mice were observed in the lung 1 and 2 days following ozone exposure. There was increased expression of heme oxygenase-1 (HO-1), a marker for oxidative stress, particularly at 48 hours. Lung tissue and bronchoalveolar lavage (BAL) fluid were collected 24 and 48 hours post-ozone exposure in SP-C^{-/-} mice and 14 days later in WT and FXR^{-/-} mice. BAL protein levels in wild type (WT) and FXR^{-/-} mice were significantly different from control following ozone and NM exposure. These findings may be useful in the development of therapeutics aimed at mitigating ozone and NM-induced lung inflammation and injury.

I. INTRODUCTION

The lungs are important for respiration, gas exchange and the regulation of acidity in the body. They transfer oxygen from the environment into the bloodstream, and influence innate immunity. Both of these gene knockout models regulate inflammation and were chosen to understand their effect on the immune response triggered by exposure to each of the two injury models: NM, a chemical warfare agent; and ozone, a toxic air pollutant. The goal of this experiment was to analyze the role of FXR and SP-C in pulmonary injury.

II. METHODS

To SP-C^{-/-} mice were exposed to air or ozone. BAL fluid was collected by instilling PBS (a saline solution) into the lungs through a cannula in the trachea, centrifuged, and resuspended. WT and FXR^{-/-} mice were treated with PBS or NM via intratracheal instillation. Total protein content in cell free BAL and tissue lysates was quantified using a BCA protein kit; all samples were assayed using a spectrophotometer. Lung tissue and BAL fluid was collected at 24 and 48 hours following ozone exposure in SP-C^{-/-} mice and 14 days later in WT and FXR^{-/-} mice. BAL protein assays were performed to quantify protein; more protein indicated greater injury because surfactant proteins are released after injury to keep the lungs from collapsing. Lung sections were evaluated for inflammation and injury and scored on a scale from 0 to 3 to account for the extent and severity of damage.

III. RESULTS AND DISCUSSION

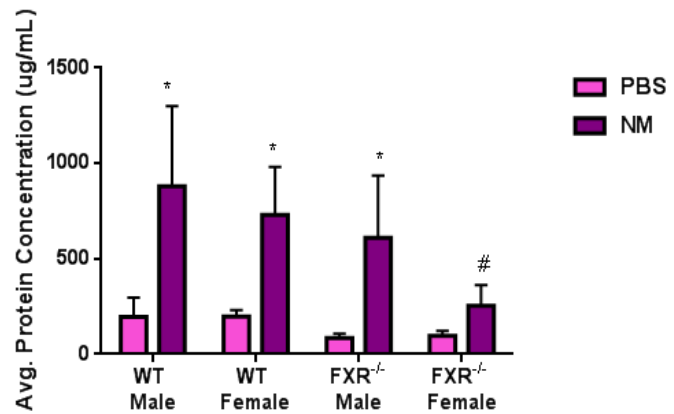


Figure 1: Figure 1. BAL protein concentrations collected 14d post-NM exposure.

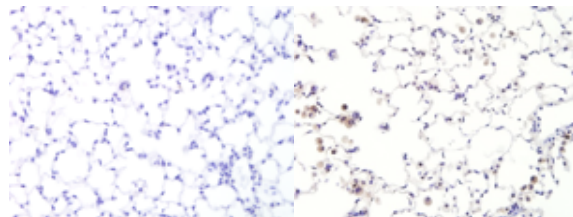


Figure 2. Macrophage populations. SP-C^{-/-} HO-1 IHC Air vs. Ozone 48 h.

Compared to control experiments, increased BAL protein concentrations were evident in mice following acute exposure to NM and ozone. In direct response to injury, pro-inflammatory macrophages accumulated and oxidative stress increased. Over time, the number of anti-inflammatory macrophages increased, indicating instigation of tissue repair. BAL protein levels were elevated following ozone and NM exposure, suggesting that FXR and SP-C modulate macrophage response, resulting in more pro-inflammatory macrophages and increased oxidative stress. Ozone initially elicits increases in iNOS pro-inflammatory macrophages and oxidative stress through the expression of heme oxygenase-1 (HO-1), a marker for oxidative stress. In FXR^{-/-} mice following NM exposure, there is a significant increase in oxidative stress and a shift toward an anti-inflammatory macrophage phenotype. SP-C and FXR are crucial genes in regulating inflammation following lung injury.

IV. ACKNOWLEDGMENTS

I would like to thank my mentors, Dr. Debra Laskin, Ms. Alexa Murray, Dr. L. Cody Smith, the Laskin and Gow Labs at the Rutgers University Ernest Mario School of Pharmacy, as well as the LSC Partners in Science program for making this research possible.

V. REFERENCES

- [1] Fredenburgh, L. E., Perrella, M. A., & Mitsialis, S. A. (2007). The Role of Heme Oxygenase-1 in Pulmonary Disease. *American Journal of Respiratory Cell and Molecular Biology*, 36(2), 158–165.
<http://doi.org/10.1165/rcmb.2006-0331TR>
- [2] Laskin, D.L., Sunil, V.R., Gardner, C.R., and Laskin, D.L. (2013). Macrophages in Tissue Injury: Agents of Defense or Destruction? *Annual Review of Pharmacology and Toxicology*, 51, 267-288.
- [3] Mosser, D. M., & Edwards, J. P. (2008). Exploring the full spectrum of macrophage activation. *Nature Reviews Immunology*, 8(12), 958–969.
<http://doi.org/10.1038/nri2448>
- [4] Sunil, V. R., Patel, K. J., Shen, J., Reimer, D., Gow, A. J., Laskin, J. D., & Laskin, D. L. (2011). Functional and inflammatory alterations in the lung following exposure of rats to nitrogen mustard. *Toxicology and Applied Pharmacology*, 250(1), 10–18.
<http://doi.org/10.1016/j.taap.2010.09.016>

A Taxonomic Morphometric Analyses between Extinct Dominican Fossilized Formicidae from the Miocene and Extant Dominican Formicidae

Alan Chen

Abstract — This study analyzes Dominican fossil-ants from the Miocene epoch (20 MYA). The objective is to infer ecosystem changes from the evolutionary change over 20 million years by comparing Miocene Formicidae fossils to modern Holocene specimens. Morphometric data, consisting of body measurements, were gathered from fossil ants and compared to those of modern ants. The comparison showed an overall decrease of Formicidae diversity. There are also some traits that collectively exhibited evolution over time. Many traits, however, remained static. The evolutionary changes observed indicate some driving environmental change which exerted selective pressures—forcing adaptation. The fact that many phenotypes remained static suggests that traits remain favorable and that environmental changes over 20 million years were not dramatic.

I. INTRODUCTION

Perhaps one of the most disregarded yet fascinating ecological impacts and evolutionary stories involves the humble Formicidae, or ant. Ants are architects of the ecosystem, affecting both species diversity and density around them.¹ All Formicidae display eusocial tendencies including altruistic behaviors. Eusocial tendencies, a notorious non-morphological synapomorphy of Formicidae, has led to their expansion and dominance over the world ecosystems, including every highly populated continent today.² Ants first appeared in the fossil record about 100 million years ago during the Cretaceous.³ During the Eocene around 50 million years ago, the number of Formicidae fossils discovered dating back to this era rose significantly, suggesting the start of ant dominance.³

Formicidae fossils have been found worldwide, and significant amounts of these fossils derive from the Caribbean island of Hispaniola (Barden 2016). Hispaniola is home to a tropical environment making the island a prime location for biological diversity and evolution. Furthermore, Hispaniola splitting from the Greater Antilles allows for geographic isolation leading to allopatric speciation. The island also allows for limited genetic drift, as all alleles present on the island will not deviate. Amber, fossilized tree resin, is abundant in Hispaniola. This resin provides near immaculate preservation of morphological details on ants, essentially providing a window into the Miocene (Sherratt et al. 2015). This study looks at previously described Formicidae fossils from Hispaniola dating back to the Miocene. Morphometric analyses consisted mainly of incorporating head length, head width, eye length, eye width, mandible length, procoxa length, Weber's length (length of mesosoma), and the cephalic index (ratio of head length to head width). Analyses were conducted on all extant discoveries of the genera present today on Hispaniola as well as during the early Miocene; a further restriction of data to only Hispaniolan fossils was also imposed.

Fossil ants and extant ants have not been used in studies together. Moreover, polymorphism in fossil Formicidae, temporal information, and geographic and ecosystem distribution depend on fossil data to determine. While there still are gaps in the fossil record, with the discovery of numerous amber fossilized Formicidae specimens in Hispaniola amber deposits, further studies to advance the

evolutionary understanding of these organisms are possible. Therefore, it is asked: Is there a significant difference between phenotypes of ancient Dominican Formicidae genera and extant genera? This study aims to infer evolutionary trends of Formicidae that have resided on Hispaniola. To sum, because evolution is responsible for the diversity of life on earth, empirical studies allow observation of evolution, and ants having a rich fossil record to study, ants were chosen as a paradigm of evolution. This aims to observe evolutionary trends over time through ants and amber.

II. METHODS

All extant species of Formicidae known on Hispaniola were compiled and sorted by genera. There were 401 extant Formicidae species found. Compiling a list of all fossilized Formicidae known followed, and was also sorted by genera. There were 96 specimens in 66 different species found, including private specimens from the Barden collection at NJIT. Both lists of genera were analyzed and an exhaustive list incorporating all Formicidae genera from the Miocene that survive today. There were 21 genera total surviving today from the Miocene.

After compiling a comprehensive list of Formicidae genera present today and in the Miocene, measurements were taken of all specimens with available measurements. These measurements included head length, head width, mandible length, eye length, eye width, procoxa length, and Weber's Length (mesonotal). Total length was not measured due to the expandability of the gaster, the last segment of the ant. Therefore, gaster lengths, as well as total length, were excluded.



Figure 2: Static phenotypical measurements and indices of Formicidae taken include the head length, head width, mandible length, eye length, eye width, procoxa length, mesonotal (Weber's) length. The only index analyzed was cephalic index. Measurements in millimeters. Images adapted from AntWeb.

Statistic approaches were considered before analysis. The final statistical output included principal component analyses between all extant and extinct Formicidae on Hispaniola to determine morphospace occupied. A paired t-test for each morphometric measurement between all genera, giving an indication of the ecological niche in which the Formicidae resides as well as evolutionary changes in head shape in each genera.

III. RESULTS AND DISCUSSION

Evolution was shown not only occurring within a genus but on the island community of Formicidae as a collective. A paired 2-tail t-test was ran between all phenotypical features. Phenotypical adaptations were seen within the island Formicidae community as a collective. There was a significant difference between extinct and extant head lengths, head widths, Weber's (mesonotal) lengths, and

cephalic indices of extinct and extant ants. The data suggested head sizes increasing over time. This bigger ant trend is also seen with Weber's length, which showed adaptation to become longer and larger. However, a limitation of this argument stems from the sampling error. It cannot be assumed that all extinct fossils have been accounted for, therefore the increase in head size is only a proposal. This applies to Weber's length as well. While the data indicate that the mesonotal length evolved to become larger, there could still be undescribed ants, which could deviate the mean of the extinct ants in an upwards direction.

Comparison of Extant to Extinct Ant Diversity by Morphological Feature

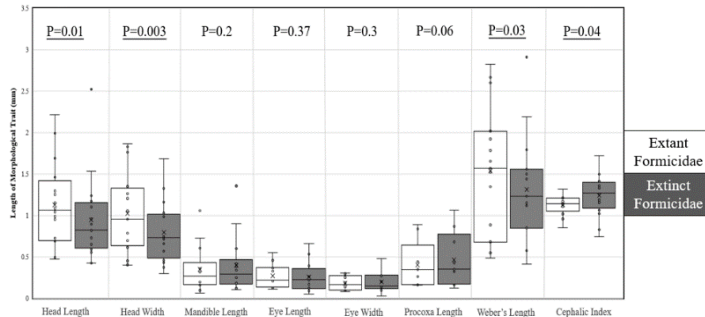


Figure 3: Each genus' morphology was averaged to create 1 data point. This is a comparison between averages of all genera within 1 measurement between the extant and extinct ants. P values from Paired 2-tail t-tests displayed.

The only collective shift that is assumed to be completely verified regards the cephalic index. The cephalic index of Miocene ants showed higher diversity and spread a larger range than modern Holocene ants. There was a significant difference of $p=0.04$ with extinct ants having a larger cephalic index than modern ants—indicating their heads were generally more elongated, on average across genera. Furthermore, because the morphospace occupation of extinct ants transcends that of extant ants, it can be concluded the diversity of head shape has decreased. The current interquartile range of cephalic index is extremely narrow, and centering just over 1. This suggests that head sizes have evolved from many diverse niches and converged on one generally favorable head shape that is only slightly elongated vertically, but mainly circular or square. This indicates the presence of a selective factor that induced this evolutionary change.

The multivariate statistical technique Principal Component Analyses (PCA) were ran on each genus. The variables included all measurements excluding the cephalic index. Presented to the left in Figure 4 is the principal component analysis for all ants discovered from the Miocene and modern ants on Hispaniola. Because the extant Formicidae plot occupies less morphospace than the extinct Formicidae, which extends beyond the morphospace of the extant population, it can be concluded that variation has decreased over the 20 million years. This indicates an environmental shift or selective pressure that caused natural selection to favor ants of a specific phenotype within the extant ants. Many extreme ants, indicated by the outermost points on the extinct morphospace plot, have either evolved to converge onto extant phenotypes or have become entirely extinct. This indicates evolution occurring on Hispaniola over the 20 million years since the Miocene, driven by selective pressures.

PCA plots also supported this shift in diversity. The principal component analysis ran between select genera including *Anochetus*, *Odontomachus*, *Platythyrea*, *Pheidole*, and *Pseudomyrmex* showed extant and extinct ants occupying differing morphospace. These five genera, selected from 21, showed almost no overlap in morphospace. This indicates that the ancient Miocene environment on Hispaniola were conducive towards certain morphotypes. However, as the environment slightly shifted, many morphotypes were selected

Principal Component Analysis Morphospace Distribution

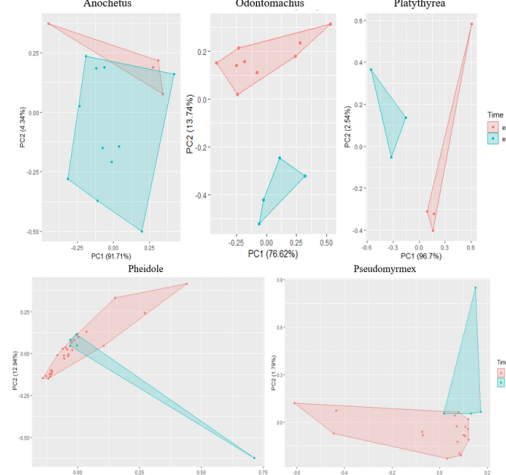


Figure 4: Principal component analysis between select Formicidae genera on Hispaniola. Red dots represent extant species while blue dots represent extinct species. Results indicate shift and reduction in Formicidae diversity over time.

resulting in the success and radiation of Formicidae belonging to other niches

The study presented here exemplifies the intricate nature of evolution, especially when studied in the microcosm of the world of Formicidae.

Results indicate

the reduction in diversity of overall ant morphospace on Hispaniola, especially including cephalic indices and overall head shape, perhaps due to selective pressures on the island as a whole. Furthermore, there is variation in how different genus compositions have changed over time. Evolutionary patterns from the Miocene to the Holocene could be due to the gradual cooling of the global climate. The gradual cooling may not have been favorable towards extremes along the spectrum of Formicidae phenotypes and morphology. Selective pressures are not limited to this, however. It is further hypothesized that anthropological involvement and invasion in Haiti and the Dominican Republic have contributed to the overall decrease in ant variation on Hispaniola. This principle holds true for the Earth's ecology as a whole, where humans have exacerbated the rate of evolution. It is urged that further studies not only confirm the findings of this study regarding morphometrics by acquiring more fossil and extant data and further analyzing for trends, but also delve into the potential of human involvement in the extinction of Formicidae species on Hispaniola, and the global biosphere as a whole.

IV. ACKNOWLEDGMENTS

I'd like to thank Dr. Phillip Barden, Ms. Amina Siraj, and the Barden Lab at NJIT for guiding my work and creating a conducive environment for my research. I'd also like to thank the Livingston High School Science Research Program with special thanks to Dr. Dorine Starace, Eric Weis, Alexander Kuziola, Mary Kaspriskie, Dr. Nuni-lyn Walsh, Mary Walmsley, and peers who have guided my work. Furthermore, I'd like to thank the NJIT Provost Summer Research High School Internship Program with special thanks to Ms. Angela Retino. I also extend my gratitude to my parents, Kevin and Vivian Chen.

V. REFERENCES

- [1] Tidyman, William E., and Katherine A. Rauen. "The RASopathies: Syndromes of Ras/MAPK Pathway Dysregulation." Neurofibromatosis Type 1, 2012, pp. 497–511, doi:10.1007/978-3-642-32864-0_32.
- [2] Busson, D, and A M Pret. "GAL4/UAS Targeted Gene Expression for Studying *Drosophila* Hedgehog Signaling." Methods in Molecular Biology (Clifton, N.J.), U.S. National Library

Change in Drosophila Receptor Activity and Contraceptive Pill Efficiency Due to Antibiotics

Emily Choe

Abstract — The increase in the use of contraceptive pills is raising the question of the effect of antibiotics. Although some warning messages inform the public about the effect of antibiotics on birth control, uncertainties regarding the specificity, magnitude, and lasting consequences of the effect on contraceptives prevail. This study tested the effect of antibiotics on the contraceptive pill Minulet, consisting of estrogen and gestodene. Penicillin, Cephalosporin, Macrolide, and Non-steroidal anti-inflammatory antibiotics were used. These selected antibiotics are some of the most commonly used drugs for multiple widespread illnesses. Drosophila (fruit flies) were utilized as estrogen and Drosophila Estrogen-Related Receptor (dERR) are essential to Drosophila growth after the pupa stage [5]. This study examined whether the antibiotics affect the Drosophila by disassembling estrogen or hindering the development of dERR itself, as well as whether there are lasting effects. The results revealed that regardless of the order of exposure, there are negative effects on the birth control pill when taken with antibiotics. However, while the estrogen could be affected by the antibiotics, the dERR had not been affected. Therefore, the antibiotics decrease the effectiveness of the contraceptive pills when taken together but there are no lasting consequences.

I. METHODS

This study tested the effect of antibiotics on the contraceptive pill Minulet, consisting of estrogen and gestodene. Penicillin, Cephalosporin, Macrolide, and Non-steroidal anti-inflammatory antibiotics were used. The antibiotics used in the experiment were procured for research, and the contraceptive pill was bought in a pharmacy.

The Drosophila were fed stock food [6] to which the appropriate antibiotics and/or pill were added. The amount of medicine added for powder was around half or one-third of the amount an adult should take each dose per day, and the amount for capsules or pills was the amount of a single tablet. 5ml of each mixture was put in each container for the fruit flies. The food was then put at room temperature to set.

Fruit flies were distributed to separate bottles using cooling anesthesia [7]. If needed, the flies were sorted by sex using a brush then put in respective containers directly while still unconscious in the freezer.

II. PARTICIPANTS/ ORGANIZATIONS

The experiment was executed by Emily Choe in a lab in Seoul, South Korea with my mentors, Joong-Soo Han and Laura Hajdukiewicz. They helped me in the planning and finalizing processes, guiding me through aspects of the study that were challenging.

The Drosophila were originally obtained from Biozoa Biological Supply (Korea).

III. EXPERIMENTAL DESIGN

Around 10 sets of virgin female and male fruit flies were used for each experiment. The flies and their food were all kept at

room temperature without excessive exposure to sunlight during the experiments.

Drosophila were tested in control with the antibiotics, contraception, and both through 14 days for each experiment. The larva and pupae on the wall and imago flies were counted in experiments. The pupae were counted by marking the newly

formed pupae each day with a different color on the outside of the breeding container.

IV. MEASUREMENTS/ DATA ANALYSIS

Antibiotics tended to decrease the survival of adult Drosophila, with the lowest being Pamoxin female survival rate of 16.7% compared to control's 66.7%.

Similarly, control's survival rate was 77.8% compared to 10.0% of when adult Drosophila was exposed to contraception. However, the exposure to the contraceptive pill quickened and magnified the formation of the pupae and growth into adult, resulting in more than 50% more growth into pupa than the controls. Therefore, while exposure to excess estrogen decreased survival of the initial generation, it had a positive effect on the growth of the following generation.

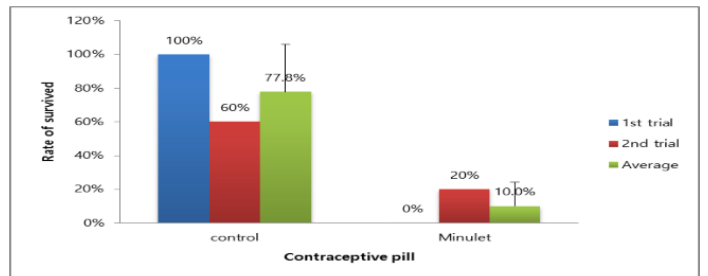


Figure 1. The survival rate and mean survival rate for adult Drosophila when exposed to the contraceptive pill Minulet. (mean \pm SD)

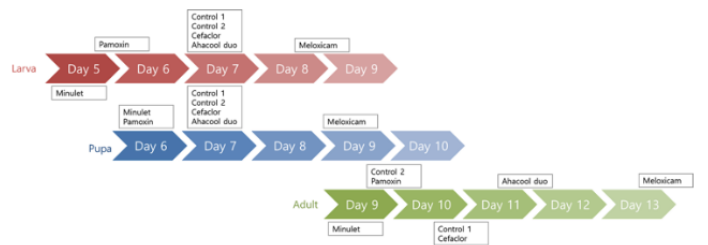


Figure 2. The time of appearance for larva, pupa, and adult from the Drosophila exposed to antibiotics and the contraceptive pill Minulet.

On the other hand, the antibiotics exposure did not have a clear pattern, as Pamoxin and Ahacool duo formed pupae at a faster rate than the control's whereas Cefaclor had a smaller range and a slower rate than the control's and Minulet.

Some antibiotics such as Ahacool duo reduced the speed of growth slightly, with its adult Drosophila appearing an average of two days after the control. This negative effect was either the antibiotics dismantling the process of Drosophila Estrogen-Related Receptor (dERR) development or the lack of estrogen required for Drosophila development because of antibiotics breaking down estrogen.

The addition of the contraceptive pill to antibiotics decreased growth rates slightly compared to separate exposure to antibiotics and contraceptive pill. The ratio of adult over pupa when exposed to both Pamoxin and Minulet was 2.3% lower than that of only Pamoxin, with both more than 50% lower than the control.

Figure 3. The number of pupae formed by the Drosophila exposed to both antibiotics and contraceptive pill and its rate of eclosion to adult Drosophila from pupae.

When exposing the second generation of fruit flies nurtured in antibiotics to the contraceptive pill, the overall growth and development accelerated by the exposure to excess estrogen with the contraceptive pill compared to control.

The exposure to antibiotics after Minulet augmented the growth into pupae more than exposure to only antibiotics, each resulting in more than 5 times the number of exposure to only antibiotics. However, there is a slight reduction in the growth into adult from pupae.

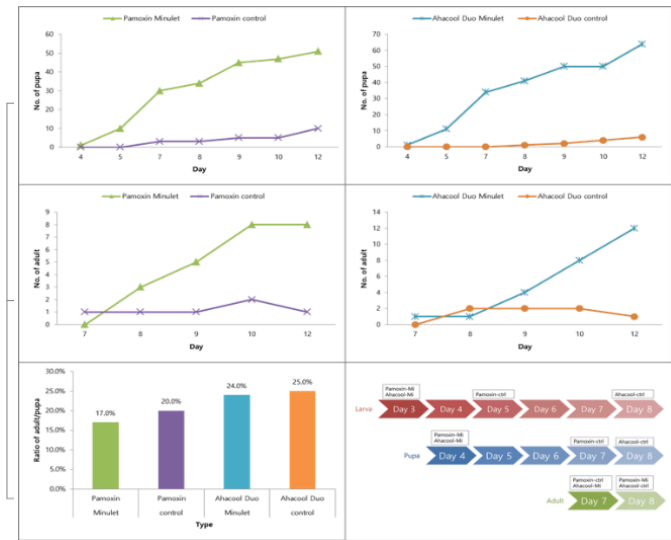


Figure 4. The numbers, rates, and appearance time of pupae and adult Drosophila exposed to contraceptive pill after antibiotics.

V. RESULTS/ DISCUSSION

Regardless of the order, exposure to both antibiotics and contraceptive reduces the effectiveness of both, as seen in the change from positive to negative effect of number of pupae and no effect to negative effect on the ratio of adult over pupa from the exposure to only the contraceptive pill to the concurrent exposure to Minulet and antibiotics. If the receptors were influenced by the exposure to the antibiotics, there should be an impact on the Drosophila that were first exposed to antibiotics then to the contraceptive pill, but there was not a large effect on the Drosophila exposed to the contraceptive pill after being exposed to antibiotics. Similarly, the Drosophila exposed to antibiotics after the contraceptive pill did not have a large change.

Therefore, the efficacy of the contraceptive pill decreases when exposed to the antibiotics at the same time, but there is no lasting negative effect.

The experiment tested for a general understanding of the influence of antibiotics on the contraceptive pill. There needs to be more work done in checking how each type of antibiotics influences the contraceptive pill, both for when taken together and for lasting consequences. Also, the study was not able to take into account the effect of gestodene, another constituent of Minulet.

Stage	Exposure				
	Minulet	Antibiotics	Minulet and Antibiotics	Antibiotics to Minulet	Minulet to Antibiotics
Adult	Negative effect	No effect	Negative effect	-----	-----
Pupa (Estrogen receptor)	Positive effect	No effect	No effect/ Small negative effect	Positive effect	Positive effect
Ratio of Adult over Pupa (Estrogen)	No effect	Negative effect	Negative effect	Negative effect	Negative effect

Table 1. The Effect of Antibiotics and Contraceptive Pill on the Effectiveness of dERR and Estrogen in Drosophila

VI. REFERENCES

- [1] Kavanaugh, M. L., Jerman, J., and Finer, L. B. "Changes in use of long-acting reversible contraceptive methods among United States women, 2009-2012." Guttmacher Institute. (2015) DOI: <https://doi.org/10.1097/AOG.0000000000001094>
- [2] Outpatient Antibiotic Prescriptions, United States, 2014. CDC Foundation. (2014) <https://www.cdc.gov/antibiotic-use/>
- [3] Department of Obstetrics and Gynecology. "Oral contraceptive efficacy and antibiotic interaction: a myth debunked." J Am Acad Dermatol. (2002) <https://www.ncbi.nlm.nih.gov/pubmed/12063491>
- [4] "Will antibiotics stop my contraception working?" NHS choices. (2016) <https://www.nhs.uk/conditions/contraception-guide/>
- [5] Tennenbaum, J. M., Baker, K. D., Lam, G., Evans, J., and Thummel, C. S. "The Drosophila Estrogen-Related Receptor Directs a Metabolic Switch That Supports Developmental Growth." PMC. (2011) <https://www.ncbi.nlm.nih.gov/pmc/articles/PMC3072597/>
- [6] Bloomington Drosophila Stock Center. "Cornmeal, Sucrose and Yeast Medium." <https://bdsc.indiana.edu/information/recipes/harvardfood.html>
- [7] Pete Geiger. *Drosophila Melanogaster and Mendelian Genetics*. "Anesthetizing flies by cooling." "Transferring flies from one vial to another." <http://depts.washington.edu/cberglab.wordpress/outreach/a-n-introduction-to-fruit-flies/>

Facile Synthesis, Characterization and Electrochemical Testing of Lithium-ion battery cathode material, $\text{LiNi}_{0.5}\text{Mn}_{1.5}\text{O}_4$

Vasu Kaker, M.V. Reddy (PhD)

Abstract — Lithium ion batteries (LIBs) are widely used in electronic devices such as mobile phones and laptops as well as electric vehicles. LIBs have the highest specific energy (amount of energy stored per kilogram of battery or electric material) out of all commercialized battery options. The cathode material used in LIBs is typically Lithium Cobalt Oxide (LiCoO_2) of which the major chemical constituent is cobalt: a toxic, expensive, unsustainably sourced metal. In this study, we synthesised and evaluated the performance of an alternative, cobalt free cathode material, Lithium Nickel Manganese Oxide ($\text{LiNi}_{0.5}\text{Mn}_{1.5}\text{O}_4$). It is much cheaper, less toxic, and has the potential to match the specific energy of Lithium Cobalt Oxide (LiCoO_2) cathodes. $\text{LiNi}_{0.5}\text{Mn}_{1.5}\text{O}_4$ was successfully synthesized through a new molten salt synthesis where precursors of LiOH , LiCl , Ni(OH)_2 and either Mn_2O_3 (Mn^{3+}) or Mn_2SO_4 (Mn^{2+}) were mixed in a crucible and heated in a furnace. The sample was later characterized via X-Ray Diffraction and Scanning Electron Microscopy imaging. Battery cells were then assembled and subjected to electrochemical testing at room temperature. Our results showed a reversible capacity of 120 milliampere hours per gram (mAh/g) at 0.1 Coulombs (C) rate, and a discharge voltage of 4.6 Volts. The synthesized material exhibited a comparable specific energy to LiCoO_2 .

I. INTRODUCTION

Lithium ion batteries (LIBs) traditionally consist of four main components: a graphite anode, a metal oxide cathode, a separator material and a liquid electrolyte. These batteries work by shuttling lithium ions from the metal oxide cathode to the graphite anode through the electrolyte. This releases electrons in the process at high voltages of 3-4 Volts (V) in order to power or charge a device. Cathodes typically account for almost 40% of battery mass, therefore, innovations in cathode materials can dramatically impact the cost, specific energy, and toxicity of LIBs [1]. The most common cathode material used is Lithium Cobalt Oxide (LiCoO_2). Other common variations including $\text{Li}(\text{Ni}_{1/3}\text{Mn}_{1/3}\text{Co}_{1/3})\text{O}_2$ (NMC) also use cobalt [as cobalt generally allows for a high specific energy. However, cobalt is expensive with prices ranging from \$41000 to \$81000 per ton [2][3]. This is 4-8 times higher than the cost of Nickel and 20-40 times the higher than the cost of Manganese [4][5]. Moreover, 70% of the world's cobalt comes from mines in the Democratic Republic of Congo (DRC). Many such mines are controlled by warlords, rendering supply to be unstable. Cobalt mining in the DRC also involves child labor, causing children severe respiratory problems and systemic poisoning as cobalt is highly toxic [6]. These factors make cobalt usage in Li-ion batteries unsustainable. Nickel and manganese are less toxic, significantly cheaper, and are sourced in a more sustainable manner.

A potential cathode material alternative is lithium manganese oxide (LiMn_2O_4). However, using the material limits battery voltage to 4V, decreasing specific energy (amount of energy a cathode material can hold). LiMn_2O_4 also has poor structural stability, therefore losing capacity quickly. Adding Nickel helps to increase voltage to 4.6V whilst improving capacity retention over a number of cycles (the number of full charges and discharges cell undergoes, done to simulate commercial application) as nickel doping stabilizes the crystal structures [6]. Hence this project focused on the variant $\text{LiNi}_{0.5}\text{Mn}_{1.5}\text{O}_4$ which contains significantly less toxic metals whose mining does not involve the child labor that a LiCoO_2 cathode would. We devised

and tested a synthetic route which enables high specific energy and capacity retention, producing a feasible alternative to LiCoO_2 .

II. METHODS

Material Synthesis and Cathode Fabrication:

An improved molten salt method was used to fabricate the cathode's active material $\text{LiNi}_{0.5}\text{Mn}_{1.5}\text{O}_4$. The method entails the melting of salts in order to release their ions from ionic bonds so that they may easily react. In batch 1, precursors of LiOH , LiCl , Ni(OH)_2 , and Mn_2O_3 (Mn^{3+}) were mixed in crucibles 1 & 2 in the ratios of 4:2:3. In batch 2, the same procedure was followed substituting Mn_2O_3 for Mn_2SO_4 (Mn^{2+}). All crucibles were heated at 900°C for 3 hours. Crucibles 2 of both batches were reheated at 850 °C under identical conditions. Excess oxygen was present in the furnace.



Figure 1 (above): Predicted reaction with Mn_2O_3

Following this, the synthesized material was mixed with Super P Carbon Black (increases electrical conductivity) and Polyvinyl Fluoride (acts as binder), in the ratio of 70:15:15. The mixture was then dispersed ultrasonically in N-methyl Pyridine (NMP) solvent. The resulting slurry was coated onto aluminum foil and dried at 80 °C for 10 hours to remove the NMP solvent. Electrodes were cut out of the foil.

III. MEASUREMENTS

Material Characterization:

Crystal structure and morphology (microscopic characteristics of material) were evaluated using X-ray diffraction and Scanning electron microscopy (SEM) imaging. Lattice parameters were evaluated using TOPAS.

Battery Cell Testing:

The battery half-cells consisting of the fabricated cathode // 1MLiPF6 electrolyte (EC:DEC) // Polymer separator // Lithium metal foil, were assembled in a glove box with an inert Argon atmosphere. The cell was in a CR2016 coin cell configuration and subjected to galvanostatic testing in a Bitrode Battery Tester to determine capacity. Cyclic voltammetry in a Biologic Macpile instrument was conducted to determine cell voltage [7].

IV. RESULTS AND DISCUSSION

X-Ray Diffraction (XRD) patterns for the sample prepared are shown in Fig. 2. The crystal also has a fixed lattice parameter value of $a=8.024 \text{ \AA}$ (angstrom). The XRD patterns of $\text{LiNi}_{0.5}\text{Mn}_{1.5}\text{O}_4$ synthesized with Mn_2O_3 (Fig. 2) match with reported values of the spinel-based material, suggesting that the spinel structure was formed [8]. Moreover, the SEM image (Fig. 4) indicates good morphology with small, consistent particle sizes which are conducive to battery performance.

While the same material synthesized with Mn_2SO_4 shows similarities to the literature XRD values (figures not shown), it also shows a mixture of NiO and $\text{LiNi}_{0.5}\text{Mn}_{1.5}\text{O}_4$ phases which indicates that the crystal structure of the material in the batch is not in a single phase. SEM imaging (Fig. 3) also indicates inconsistent morphology, suggesting the same.

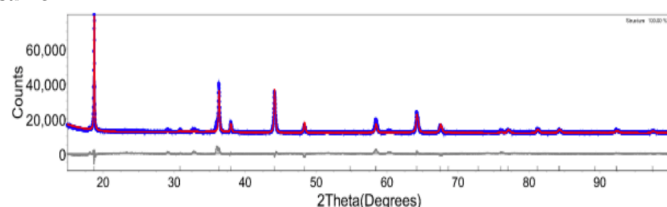


Figure 2 (above): XRD Patterns of $\text{LiNi}_{0.5}\text{Mn}_{1.5}\text{O}_4$ prepared with Mn_2O_3

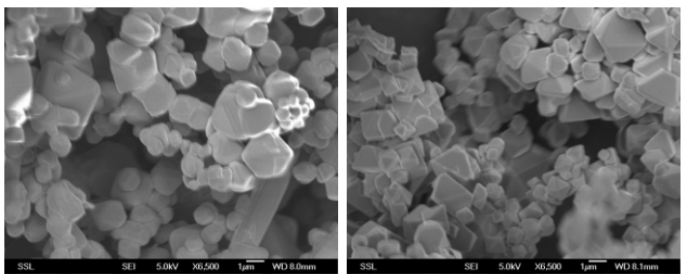


Figure 3-4 (from left to right) SEM Imaging of material prepared with Mn_2SO_4 (left) and Mn_2O_3 (right) at 900°C. 6500x magnification used.

Electrochemical Performance of $LiNi_{0.5}Mn_{1.5}O_4$ by galvanostatic cycling and cyclic voltammetry are shown in Fig. 5-6.

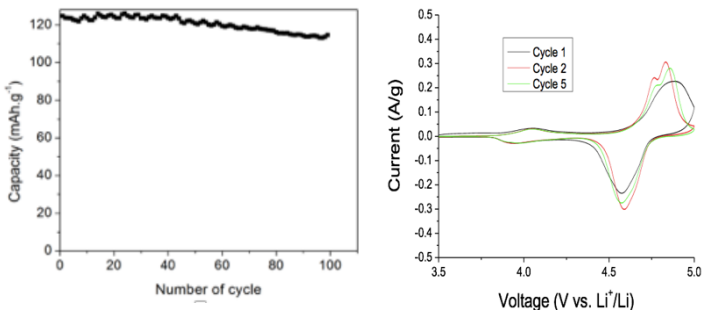


Figure 5-6 (from left to right) Capacity versus cycle number plot (cycled from 3.5 to 4.8V) and Cyclic Voltammetry curve (scan rate: 0.058mV/sec). Both curves are of cells assembled from $LiNi_{0.5}Mn_{1.5}O_4$ synthesized from Mn_2O_3 precursor that was not reheated.

As shown by the Cyclic Voltammetry Curve (Fig. 6), the cathode has a charge/oxidation voltage peak of 4.8V and discharge/reduction peak at 4.6V. The compound exhibits a reversible capacity of 122 mAh/g at 0.1C rate. Over the course of 100 cycles the capacity drops to 114 mAh/g. This indicates excellent capacity retention of 93%, comparable to most commercially used cathode materials. Thus the initial specific energy of synthesized $LiNi_{0.5}Mn_{1.5}O_4$ cathode calculated by:

$$\text{Specific Energy (Wh/kg)} = \text{Voltage (V)} * \text{Specific Capacity (Ah/kg)}$$

Figure 7 (above) Specific Energy Equation

is approximately 561 Wh (watt hours)/kg. This is slightly higher than a Lithium Cobalt Oxide cathode which has a discharge voltage of 3.7V, a practical capacity limit of 150 mAh/g, (8) and thus a slightly lower Specific Energy of 555Wh/kg. If the synthesized material were to replace the $LiCoO_2$ cathode in the same battery, the battery would provide approximately the same amount of energy per unit mass, given the similarity in the two materials' specific energy.

V. CONCLUSION

In conclusion, the crystalline $LiNi_{0.5}Mn_{1.5}O_4$ has been successfully synthesized through a facile molten salt method. It was demonstrated that precursors Mn_2O_3 , $LiOH$, $LiCl$, and $Ni(OH)_2$ heated at of 900°C for 3 hours produced the desired morphology as indicated by XRD patterns and SEM Techniques. The electrochemical tests indicate that the material produced a discharge voltage higher than conventional Li-ion batteries and has a specific energy of 561 Wh/kg, which matches the $LiCoO_2$ cathode. Moreover, the material costs less than a quarter the price of $LiCoO_2$. These characteristics in addition to obviating the need to unsustainably source cobalt indicate that our synthetic route producing $LiNi_{0.5}Mn_{1.5}O_4$ is a viable alternative to the commercially used $LiCoO_2$ cathode.

The next step would be to test this material in a Li-ion 18650 cell for commercial applications. Future research would focus on enhancing this cathode material's energy storage capacity and electrochemical stability by introducing glycine to produce the material's nanoparticle form.

VI. REFERENCES

- [1] Belmont, CA: Wadsworth, 1993, pp. 123–135.
- [2] M.V. Reddy, G.V. Subba Rao, B.V. R. Chowdari "Metal oxides and oxysalts as anode materials for lithium ion batteries" *Chemical Reviews* 113(2013)5364-5457Y. Yorozu, M. Hirano, K. Oka, and Y. Tagawa, "Electron spectroscopy studies on magneto-optical media and plastic substrate interfaces (Translation Journals style)," *IEEE Transl. J. Magn.Jpn.*, vol. 2, Aug. 1987, pp. 740–741 [Dig. 9th Annu. Conf. Magnetics Japan, 1982, p. 301].
- [3] King, A. (2018). Battery builders get the cobalt blues. *ChemistryWorld*.
- [4] Nickel History | Markets Insider. (2019, January 13).
- [5] Manganese Price | Metalary (2019, January 13). environment. (2018, March 6). *CBSNews*
- [7] Li, G., Ikuta, H., Uchida, T., Wakihara, M. (1996). The spinel phases $LiM_xMn_{2-x}O$ ($M = Co, Cr, Ni$) as the cathode for rechargeable lithium batteries. *Journal of Electroanalytical Chemistry*, 143(1), 178-182.
- [8] Birk, C., Mcturk, E., Roberts, M., & Bruce, P.G. (2015). A Parametric Open Circuit Voltage Model for Lithium Ion Batteries. *Journal of the Electrochemical Society*, 162(12), 2271-2280
- [9] Xue, Y., Wang, Z., Zheng, L., Yu, F., Liu, B., Zhang, Y., & Ke, K. (2015). Investigation on preparation and performance of spinel $LiNi0.5Mn1.5O_4$ with different microstructures for lithium-ion batteries. *Scientific Reports*, 5(1).
- [10] Cui, Y. (2010, September 29). Energy Tutorial: Battery Storage 101

Fractal Analysis of Enzyme Active Site

Kim Min Jae

Abstract — Enzymes can only react with specific substrates that enter their active sites. However, daily observations lead us to conclude that substrates find their target enzymes in a matter of minutes upon being accepted into the body. To explain how substrates are able to find enzymatic active sites in such an efficient manner, it was hypothesized that enzymes would have higher fractal dimensions in regions adjacent or leading to their active sites. This followed from the conjecture that high-fractal surfaces would have higher interactivity with surrounding solvent. Three PDB files were extracted from the RSCB Protein Data Bank and each was divided into 1,000 cuboid regions. The fractal dimensions of each of these regions were calculated and visualized. The visualizations illustrated that enzymatic regions leading into the active site had high fractal dimensions, while regions adjacent to the active site were observed to not necessarily have high fractal values.

I. BACKGROUND INFORMATION

Fractals are self-similar shapes i.e. shapes in which the same pattern repeats itself on smaller scales. Proteins were found to exhibit similar, self-affine qualities i.e. protein surfaces have fractal dimensions. The fractal nature of proteins can help us understand the connection between their macroscopic characteristics and atomic interactions [1].

II. METHODS

PDB files—files containing the structural information of proteins—were obtained from the RSCB Protein Data Bank. Visualizations and molecular analysis was done with Chimera, and additional refinement algorithms were coded using Wolfram Mathematica.

The PDB files of the following enzymes were analyzed:

1. Carbonic Anhydrase (1CA2): As a diffusion-limited enzyme, carbonic anhydrase was chosen to represent enzymes that have high turnover numbers.
2. Bovine Liver Rhodanese (1RHD): Another enzyme with a relatively high turnover number, bovine liver rhodanese was chosen to be compared with carbonic anhydrase. Also, rhodanese' substrate cyanide is highly soluble, thus its movement is well approximated by the solvent.
3. Porcine Pancreatic Elastase (3HGN): Porcine pancreatic elastase clips amino acids within the pancreas. Transport through water being an essential to this enzyme, it was deemed that porcine pancreatic elastase's fractal structure might shed light on the relationship between the fractal dimensions of molecular surfaces and the flow of solvent.

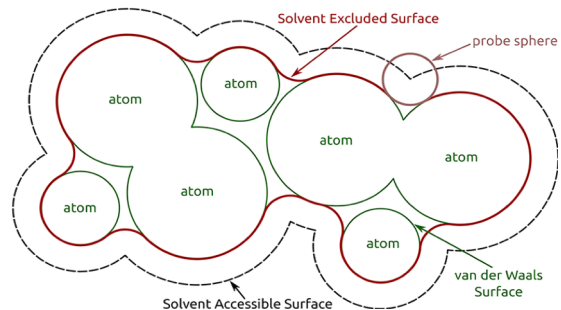
They will now be referred to using the PDB ID codes indicated in parentheses above.

Coordinates of atoms part of the enzyme were extracted from each PDB file. These extracted structures were dissected into 1,000 similar cuboid regions, which were recorded into separate PDB files. The fractal dimension of each of these enzyme regions, which

now had corresponding PDB files, were calculated using the following equation [2]:

$$d_f = 2 - \frac{d\log(\text{SES})}{d\log(r)}. \quad (1)$$

"SES" stands for the solvent excluded area of an enzyme, which is calculated by rolling a spherical probe over the enzyme's surface; "r" is the radius of this probe in angstroms (100 pm).



Molecular surfaces were designated "fractal indices," values proportionate to the squared values of the surfaces' fractal

Figure 1. Molecular Surfaces [3]

dimensions. These values were recorded onto each enzyme's PDB file and color-coded using Chimera. All molecular surfaces were created using a probe with a radius of 80 pm.

Markers of active sites were assigned unrealistically high fractal indices, and thus colored purple. The location of the zinc atom was used as a marker for the active site of 1CA2; S-Mercaptocysteine, 1RHD [4,5]; FRW, 3HGN.

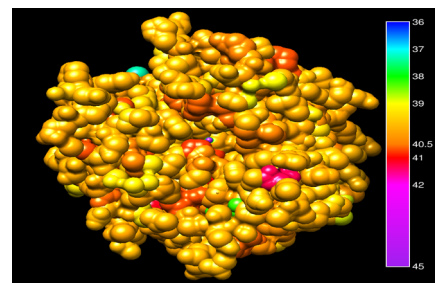


Figure 2. Visualization with Downward Increasing Spectrum

III. DATA ANALYSIS

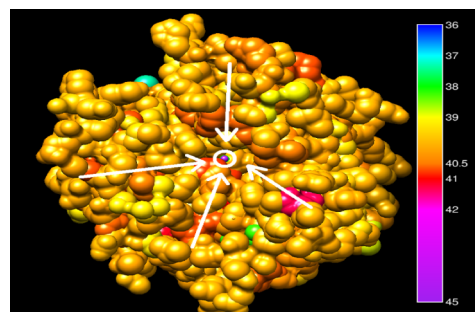


Figure 3. 1CA2

The zinc atom indicating 1CA2's active site is located in a big cavity. The fractal indices of the surfaces within this cavity—that is, adjacent to the active site—are around 40, similar to the mean fractal index for the whole protein (Figure 4). In addition, there are high-fractal pathways with indices 40.5 to 41 leading into this cavity (Figure 3).

The active site of 1RHD is also inside a cavity, albeit smaller than that of 1CA2. The fractal indices of these areas within the cavity active site are relatively low, 38-39 (Figure 5). The mean fractal index for 1RHD is 40.04.

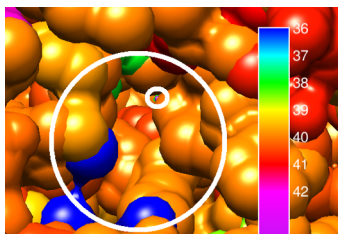


Figure 5. 1RHD

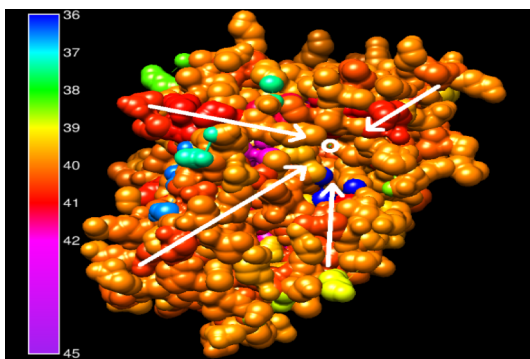


Figure 6. 1RHD

As was the case with 1CA2, solvent seems to be attracted by high-fractal regions that extend along the outer surface of the enzyme. These high-fractal surfaces would lead the solvent to the cavity, which holds the active site. Figure 6 explicitly illustrates such pathways (fractal indices around 41) that lead substrate-carrying solvent to the active site.

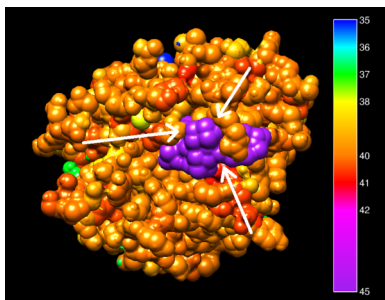


Figure 7. 3HGN

For 3HGN, high-fractal regions are encrusted inside the enzyme in areas adjacent to the active site. The visualizations illustrate the fractal values gradually getting higher as they approach the FRW inhibitor (Figure 7).

Since FRW is an inhibitor, we can expect it to block pathways leading to the active site. Thus, it makes sense that the high-fractal pathways in Figure 7 are blocked by FRW before reaching the active site. Without the inhibitor, the solvent would be able to reach the active site by following these high-fractal paths.

IV. RESULTS AND DISCUSSION

Analysis of 3 PDB structures and their regional fractal dimensions has illustrated that enzymatic regions leading to active site have relatively higher fractal dimensions. Areas adjacent to active site had a variety of fractal values.

The observational study was conducted using static PDB structures. Running Molecular Dynamics (MD) Simulations may present a more detailed picture of a protein's fractal structure and the movement of surrounding solvent in a physiological environment. This can provide deeper insight into the relationship between fractal structures and solvent flow. Such knowledge can be used in drug development as diseases such as cancer spread through the body by following the flow of solvent much like enzymatic substrates do.

V. REFERENCES

- [1] A. Banerji, *Studying Protein Interior with Fractal Dimensions*, New York: Springer, 2013, pp. 19–21.
- [2] A. A. Kaczor, R. Guixà-González, P. Carrió, C. Obiol-Pardo, M. Pastor and J. Selent, "Fractal dimension as a measure of surface roughness of G protein-coupled receptors: implications for structure and function," *Journal of Molecular Modeling*, vol. 18, no. 9, pp. 4465-4475, 2012.
- [3] C. Ferrari and S. Daberdaku, "Fast Computation of High-resolution Solvent Excluded Protein Surface with OpenMP" in *The 2018 International Conference on High Performance Computing & Simulation*, Orléans, 2018.
- [4] S. Wang and M. Volini, "Studies on the Active Site of Rhodanese," *The Journal of Biological Chemistry*, vol. 243, no. 20, p. 5465, 1968.
- [5] J. Russell, L. Weng, P. Keim and R. Heinrikson, "The covalent structure of bovine liver rhodanese. Isolation and partial structural analysis of cyanogen bromide fragments and the complete sequence of the enzyme," *The Journal of Biological Chemistry*, vol. 253, no. 22, p. 8105, 1978.

A Customized Machine Learning Pipeline to Build State-of-the-Art Audio Classifiers

Sruthi Kurada

Abstract – Audio classifiers have many real-world applications, from informing medical diagnoses to revealing automobile malfunctions. In this study, I have explored strategies to build an accurate classifier to categorize environmental sounds from the UrbanSound8K dataset. Published classifiers on this ten-class dataset only have 50-79% accuracy. Through engineering a machine learning pipeline, I have built a state-of-the-art classifier with a 99% test-set accuracy on this dataset. In order to examine the general applicability of this pipeline to build reliable classifiers on other audio datasets, I have examined its performance in differentiating four unique heart sounds and found it to be equally effective. The final heart sound classifier achieved a 98% test set accuracy.

I. INTRODUCTION

Audio classifiers categorize acoustic input based on inherent sound characteristics. Many classifiers have been created on the UrbanSound8K [1], a 10-class public dataset of 8732 city sound files. The highest performing among these classifiers achieved a 79% accuracy [2]. I sought to build a classifier with a higher accuracy on this dataset. Subsequently, I aimed to create a generalizable pipeline that enables building high performance classifiers on other audio datasets. A generalizable pipeline could be integral to the development of high-fidelity audio classifying machines for all applications.

II. METHODS

Through employing Python and the librosa library [3], audio features including Mel-frequency cepstral coefficients (MFCCs), Chroma, Mel, Contrast, and Tonnetz were extracted from the UrbanSound8K dataset. These components were used to train various machine learning classifiers using the Sci-kit learn library [4]. Classifiers included in the study were Logistic Regression (LR), Linear Discriminant Analysis (LDA), K-Nearest Neighbors (KNN), Classification and Regression Trees (CART), Naive Bayes (NB), and Support Vector Machines (SVM). These classifiers were further tuned by applying dimensionality reduction, pre-processing, hyper-parameter optimization, and data-augmentation techniques [4-5].

Accuracy was the primary metric used to quantify classifier performance. In the assessment phase, source data was randomly split (80:20 ratio) into training and testing sets. K-fold ($k=10$) cross validation was then employed on the training set, and testing was performed on the held-out test set. To assess the generalizability, the resulting best-performing pipeline on the UrbanSound8K dataset was applied to a four-class heart sound dataset [6].

III. RESULTS AND DISCUSSION

Figure 1 shows that the KNN classifier achieved the highest baseline 10-fold cross-validation accuracy rate (mean \pm S.E.M; $82.7 \pm 0.02\%$) of all of the classifiers in the study. The figure

also shows that the KNN classifier performed similarly when provided the full audio feature-set as compared to when given only MFCCs.

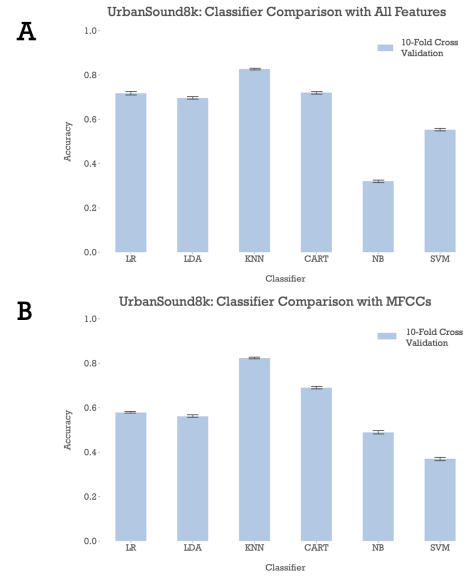


Figure 1A: Baseline classification accuracy of six classifiers with the full feature set provided (MFCCs, Chroma, Mel, Contrast, Tonnetz). Classifiers included Logistic Regression (LR), Linear Discriminant Analysis (LDA), K-Nearest Neighbors (KNN), Classification and Regression Trees (CART), Naïve Bayes (NB), and Support Vector Machines (SVM).

Figure 1B: Baseline accuracy of the same classifiers with only MFCCs as input.

Thus, I chose to employ MFCCs as the sole input to the KNN classifier before attempting pre-processing, hyper-parameter optimization, and data augmentation steps to improve its accuracy. Table 1 summarizes improvements achieved after implementing the above techniques. A $99.36 \pm 0.09\%$ cross validation accuracy was achieved on the training set by applying these three additional tuning steps. The final pipeline earned a 99.47% test set accuracy.

Baseline KNN with all features	$82.66 \pm 0.43\%$
+Only MFCCs (Dim. Red)	$82.37 \pm 0.45\%$
+Data Preprocessing	$89.00 \pm 0.44\%$
+Hyperparameter Optimization	$94.60 \pm 0.21\%$
+Data Augmentation	$99.36 \pm 0.09\%$
Test Set Performance	99.47%

Table 1: The increases in performance enabled by including dimensionality reduction, pre-processing, hyper-parameter optimization, and data augmentation in the final UrbanSound8K KNN classification pipeline enabled achieving a 99.47% test set accuracy.

Figure 2 shows the confusion matrix of the tuned KNN pipeline. The majority of the false detections observed were between the jackhammer and drilling classes.

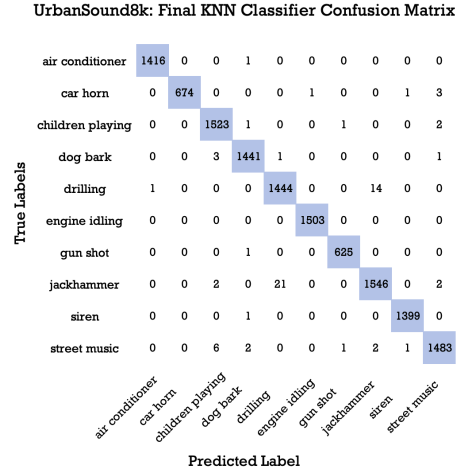


Figure 2: Confusion Matrix of the final UrbanSound8K KNN pipeline

In order to assess the pipeline's generalizability, the same procedures were applied to a separate dataset – a four-class heart sound dataset. A KNN classifier was the highest performer on the new dataset (Table 2), despite CART and LR classifiers performing better initially* (Figure 3).

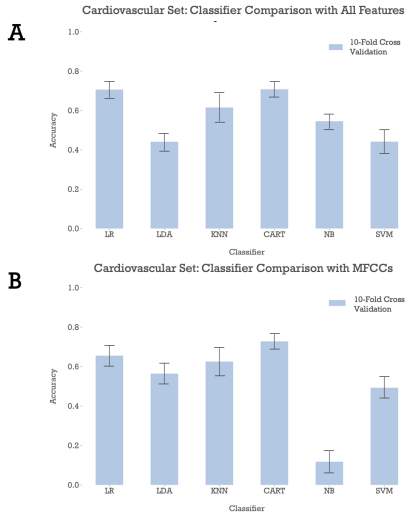


Figure 3A: Baseline cardiovascular sound classification accuracies when the full feature set is provided.

Figure 3B: Baseline accuracies of the same classifiers with only MFCCs as input.

Table 2 (following page): The stepwise boosts in accuracy achieved by implementing dimensionality reduction, pre-processing, hyper-parameter optimization, and data augmentation in the final heart sound KNN classification pipeline.

Baseline KNN with all features	$61.56 \pm 7.07\%$
+Only MFCCs (Dim. Red)	$62.56 \pm 7.10\%$
+Data Preprocessing	$71.78 \pm 4.61\%$
+Hyperparameter Optimization	$71.78 \pm 4.61\%$
+Data Augmentation	$98.48 \pm 0.09\%$
Test Set Performance	97.791%

IV. DISCUSSION

Optimized KNN pipelines were the highest performers on both datasets in this study. As shown by Figure 1 and 3, the KNN classifiers performed equally well with either the full audio feature set as input or with MFCCs as the sole input. This finding has several advantages. Not only is feature extraction faster with one input, but scaling is also more efficient and overfitting is minimized. The program's memory footprint is lowered as well. As shown in Table 1 and 2, preprocessing input data, optimizing classifier hyperparameters, and using augmented datasets were essential for achieving a high accuracy.

The above pipeline was also employed on additional audio datasets in order to further examine its generalizability [6, 7]. The pipeline achieved >90% cross-validation and test-set accuracies on these datasets as well (data not shown).

V. CONCLUSION

The above results illustrate that a ML pipeline including pre-processing, hyper-parameter optimization, and data augmentation steps can be used to build state-of-the-art audio classifiers on multiple datasets with MFCCs. This approach enables developing models with high performance and low variance while avoiding overfitting. In the future, I will explore the effectiveness of this pipeline for semi-supervised learning applications.

VI. REFERENCES

- [1] J. Salamon, C. Jacoby and J. P. Bello, "A Dataset and Taxonomy for Urban Sound Research", 22nd ACM International Conference on Multimedia, Orlando USA, Nov. 2014, pp. 1041–1044.
- [2] J. Salamon, and J. P. Bello, "Deep Convolutional Neural Networks and Data Augmentation for Environmental Sound Classification," *IEEE Signal Processing Letters*, Nov. 2016, pp. 279 – 283.
- [3] B. McFee, C. Raffel, D. Liang, D. Ellis, M. McVicar et al, "Librosa: Audio and Music Signal Analysis in Python." *Proceedings of the 14th Python in Science Conference*, July 2015, pp. 18-25.
- [4] F. Pedregosa , G. Varoquaux, A. Gramfort, V. Michel, B. Thirion, O. Grisel, M. Blondel et al, "Scikit-learn: Machine learning in Python," *Journal of Machine Learning Research*, Nov 2011, pp. 2825-2830.
- [5] B. McFee, E. Humphrey, and J.P. Bello, "A software framework for musical data augmentation." *International Society for Music Information Retrieval Conference*, Aug 2015, pp. 248-254.
- [6] P.J. Bentley, G. Nordehn, M. Coimbra, S. Mannor, R. Getz, "The PASCAL Classifying Heart Sounds Challenge 2011," [online] Available: www.peterjbentley.com/hearthchallenge/.
- [7] G. Clifford, C. Liu, B. Moody, D. Springer, I. Silva, Q. Li, and R. Mark. "Classification of normal/abnormal heart sound recordings: The PhysioNet/Computing in Cardiology Challenge 2016," *Computing in Cardiology Conference (CinC) - IEEE*, Sep. 2016, pp. 609-612.

A Rule-Based Natural Language Processing Pipeline for Anesthesia Classification from Unstructured Operative Notes

Mrunali Manjrekar, Selen Bozkurt, PhD, Anthony J. Nastasi, MHS, Catherine Curtin, MD, and Tina Hernandez-Boussard, PhD, MPH, MS

Abstract— Previous studies have shown anesthesia type administered during operations can influence postoperative pain outcomes. However, researchers cannot quickly analyze anesthesia type in large studies from electronic health records because of their unstructured data format. In this study, we show the development, implementation, and evaluation of a natural language processing (NLP) pipeline, a series of Python-programmed rules built to classify different types of anesthesia type based on textual features within the free text of operative notes. The first pipeline attained a precision score of 1 out of 1 and recall score of 0.96 out of 1 on 100 post-operative notes annotated by a clinician. After initial revision and testing on independent data, the second pipeline's overall precision score of 0.88 and recall score of 0.77 suggests a need for more robust dictionaries to match additional textual features and improved intuitive context extraction to increase accuracy.

I. INTRODUCTION

The unstructured form of clinical notes in the Electronic Health Record (EHR) limits researchers from quantitatively studying operative care for improving relevant patient-centered outcomes. Manual abstraction of large amounts of data quickly becomes unfeasible and important clinical questions remain unanswered. One such question is how the type of operative anesthesia (general, regional, and/or local) influences important outcomes. Smaller studies suggest anesthesia type can influence patient-centered outcomes, particularly pain-related outcomes [1-3]. However, anesthesia is not well coded due to the large amount of redundant information obscuring more important data; anesthesia is recorded in multiple types of notes, including operative and anesthesia notes, whose differing structures contribute to unclear extraction. As a result, the notes where anesthesia documentation is recorded require significant processing to be reliably analyzed; incorrect analysis could distort the relationship between anesthesia type and pain experienced post-surgery [4-5]. The purpose of this study is to accurately extract anesthesia records from EHR to examine the association of anesthesia type with relevant clinical outcomes. As the information on anesthesia type is embedded in the free text of clinical notes generated by clinicians, we utilized natural language processing (NLP) methods to bridge the gap between free-text and structured representations of clinical information. We thus developed a rule-NLP pipeline, a set of programmed rules to quantitatively analyze unstructured data based on certain textual characteristics [2-3], to extract and

classify anesthesia operative details from the free text of EHR notes [6-7].

II. METHODS

A rule-based NLP pipeline was developed in Python 2.7, using numpy, pandas and nltk modules [8]. The pipeline first pre-processed (lowercasing, removing punctuations) the operative notes. To segment the report, all

text between the anesthesia type header and the next header in the note was extracted in the first pipeline; however, a second pipeline developed for validation was revised to include other parts of the report by checking for the presence of anesthesia headers, successive headers, sentence delimiters, and “anesthesia” itself. For actual classification, extracted contexts were matched via dictionary mapping with target terms and their relevant anesthesia type, based on a versatile lexicon built with clinical and domain knowledge (Fig. 1).

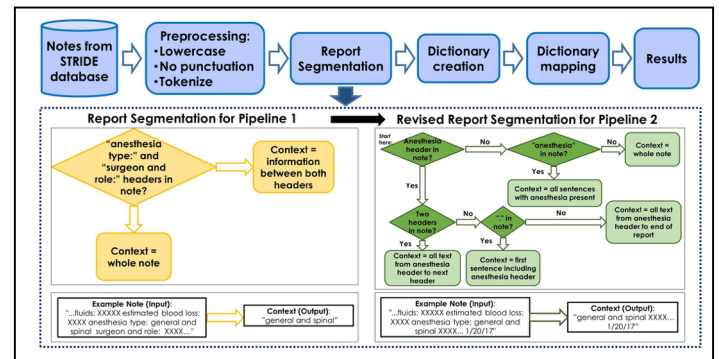


Figure 1. Proposed Pipeline Architecture. The main changes to Pipeline 2 occurred in the Report Segmentation portion of the pipeline. In the segmentation flowcharts, “context” refers to information in the note deemed relevant to be passed on to the remaining portion of the pipeline; any other portions were excluded.

Below each flowchart is an example note input and subsequent output produced as a result of that respective segmentation.

Since patients could have more than one anesthesia type and/or have multiple operation notes, the pipeline was reformatted to classify anesthesia type by patient, not note, to account for all types. This dual classification was kept in case unexpected trends arose among certain combinations and post-operative pain outcomes. The pipeline was first tested on a sample of 100 post-operative notes from EHRs at an academic medical center, annotated by a clinician [9]. The revised pipeline analyzed an independent set of 256,000 reports with no post-operative notes, comparing a random 100 report sampling with clinician annotations to determine new agreement. The first set had 100 different patients, but the second set had patients with more than one note; however, in the sample

analyzed, the 100 notes selected each came from a different patient. Performance for both pipelines was assessed with accuracy metrics including precision, recall and f1 (the harmonic average between precision and recall) scores that ranged between 0% and 100%.

III. RESULTS AND DISCUSSION

The first pipeline evaluated 100 post-operative notes, 25 from 4 *surgery* types, performing with 100% precision and 96% recall; the second pipeline evaluated a 100 operative and anesthesia procedure note sample, 20 from 5 *note* types, performing with 77% recall and 88% precision (Table 1).

Pipeline 1			
Anesthesia Type	Recall	Precision	F1
General	1	1	1
Regional	0.91	1	0.95
Local	1	1	1
Overall	0.96	1	0.98
Pipeline 2			
Anesthesia Type	Recall	Precision	F1
General	0.96	1	0.98
Regional	0.70	0.91	0.79
Local	0.67	0.73	0.70
Overall	0.77	0.88	0.83

Table 1. Metrics for 1st and 2nd pipelines, by anesthesia type (n=100 reports)

The first pipeline mismatched four notes, three of which were from a dictionary mistake marking “spinal” as “general,” not “regional,” and one from punctuation noise. Pipeline revisions included correcting dictionaries; removing punctuation, integers, and spaces; and improving context extraction. The second pipeline mismatched 23 notes due to overlooked medication names and abbreviations, such as “lidocaine” and “GET” (general endotracheal anesthesia), and ignored/misleading contexts. F1 scores by note type varied from 0.43 to 0.91, suggesting this shift in note type was responsible for these mismatches. Anesthesia procedure notes had low performance, in part due to other misleading data recorded; operative notes provided a clearer, succinct summary of the anesthesia administered during operation. Multiple anesthesia procedure notes, specifically “Airway” and “Arterial Line” types, detailed procedures not taking place in the specific human region of operation; these notes distorted the pipeline’s precision, but can be omitted for future analysis or classification of overall perioperative anesthesia type.

The pipeline’s varied accuracy metrics by different note types indicate useful material can be extracted from unstructured EHR, but will require more robust dictionaries that include more specific medication names and abbreviations; omitting less relevant types of notes, such as

“Airway and “Arterial Line” anesthesia procedure notes; and further revisions to context extraction, including exclusion of any headers where possible to reduce ambiguity and increased versatility to handle other note types for additional information. Similar pipelines with modified report segmentation methods and dictionaries can process the same notes for additional insight into other perioperative services. Overall, improved pipelines can facilitate population-based studies of patient-centered outcomes with detailed subset analysis, allowing clinicians to provide individualized care for patients. We also plan to integrate this pipeline into our EHR database so that anesthesia type is recorded automatically in a structured format instead of free-text format. Recording anesthesia type in a structured format will clarify documentation, improve follow-up, and enable its use in future studies, which may include predicting patient-centered outcomes with machine learning tools.

IV. ACKNOWLEDGEMENT

Funding: This project was supported by grant number R01HS024096 from the Agency for Healthcare Research and Quality. The content is solely the responsibility of the authors and does not necessarily represent the official views of the Agency for Healthcare Research and Quality.

I give thanks to PI Dr. Tina Hernandez-Boussard and her research group including mentor Dr. Selen Bozkurt for the support and resources to carry out this project.

V. REFERENCES

- [1] Kaufman E, Epstein JB, Gorsky M, Jackson DL, Kadari A. Preemptive analgesia and local anesthesia as a supplement to general anesthesia: a review. *Anesthesia progress*. 2005 Mar;52(1):29-38.
- [2] Ruppert V, Leurs LJ, Rieger J, Steckmeier B, Buth J, Umscheid T. Risk-adapted outcome after endovascular aortic aneurysm repair: analysis of anesthesia types based on EUROSTAR data. *Journal of Endovascular Therapy*. 2007 Feb;14(1):12-22.
- [3] Desai K, Carroll I, Asch SM et al. Utilization and effectiveness of multimodal discharge analgesia for postoperative pain management. *Journal of Surgical Research*. 2018 Aug 31;228:160-9.
- [4] Yim WW, Wheeler AJ, Curtin C, Wagner TH, Hernandez-Boussard T. Secondary use of electronic medical records for clinical research: challenges and opportunities. *Convergent science physical oncology*. 2018 Feb 12;4(1):014001.
- [5] Weiskopf NG, Hripcak G, Swaminathan S, Weng C. Defining and measuring completeness of electronic health records for secondary use. *Journal of biomedical informatics*. 2013 Oct 1;46(5):830-6.
- [6] Demner-Fushman D, Chapman WW, McDonald CJ. What can natural language processing do for clinical decision support?. *Journal of biomedical informatics*. 2009 Oct 1;42(5):760-72.
- [7] Nath C, Albaghda MS, Jonnalagadda SR. A natural language processing tool for large-scale data extraction from echocardiography reports. *PloS one*. 2016 Apr 28;11(4):e0153749.
- [8] Bozkurt S, Park JI, Rubin D, Hernandez-Boussard T. A Natural Language Processing Pipeline for Capturing Prostate Cancer Patient-Centered Outcomes. Poster presented at: AMIA 2018 Informatics Summit; 2018 March 12-15; San Francisco, CA.
- [9] Lowe HJ, Ferris TA, Hernandez PM, Weber SC. STRIDE—An integrated standards-based translational research informatics platform. In AMIA Annual Symposium Proceedings 2009 (Vol. 2009, p. 391). American Medical Informatics Association.

Ultrasensitive volumetric imaging through optical coherence tomography

Ethan J. McFarlin

Abstract— Optical coherence tomography is a non-invasive, in-vivo imaging technique based on the principle of light interferometry. This study examines the development of an OCT imaging system powered by a 1550nm fiber laser. Real-time, cross-sectional and sub-surface volumetric imaging was performed by analyzing light backscatter from different features inside samples. Spectral encoding was Fourier transformed to produce 2D depth profiles. Conclusively, results demonstrated optimum resolution with high-contrast interference patterns, thus offering near-maximum Z-axis and translational imaging quality. Future research will aim to combine existing detection sensitivity capabilities with the imaging depth of multi-photon microscopy.

I. INTRODUCTION

Laser imaging techniques have played an essential role in modern-day healthcare and are indispensable tools for screening and early detection of diseases including age-related macular degeneration and esophageal cancers [1]. In addition, the application of laser imaging techniques for brain imaging and surgical guidance is recently gaining ever increasing attention in the community. Fourier-domain optical coherence tomography (FD-OCT) stands out from other laser imaging techniques due to its unique optical sectioning capability, ultrahigh detection sensitivity, and ultrafast volumetric imaging speed [2]. The capability to noninvasively survey large tissue volumes allows more accurate assessment of early stage, focal diseases. FD-OCT achieves quantum noise limited detection sensitivity and video rate 3D microscopic imaging by using an optical heterodyne interferometer to extract signals encoded in the spectral domain, where depth information is measured by a spectrometer. Without the need for axial scanning, FD-OCT provides 50 dB signal gain and simultaneous capture of depth information after a Fourier-transformation. This study explores the development of a proof-of-principle FD-OCT imaging modality and its corresponding axial and transverse resolution capabilities.

II. MATERIALS & METHODS

To construct the system, a femtosecond erbium doped fiber laser (EDFL), optical spectrum analyzer (OSA), and a workstation equipped with Labview programs were used. The 1550nm EDFL generated optically synchronized pulses split into reference and sample arms by a 50/50 coupler. The light source was collimated and linearly polarized with a ThorLabs fiber controller before being strongly focused into a sample. Interference patterns measured between the reflected and backscattered sample waves were used to generate reflectivity profiles. After Optical dispersive Fourier transform (DFT) technology converted the spectral encoding scheme into

temporal encoding of depth information, Gaussian waves in the frequency domain were turned into Soliton in the time domain. Full width half maximum (FWHM) calculations combined with the constant speed of light were then used to determine the smallest spatial increment the microscope could resolve.

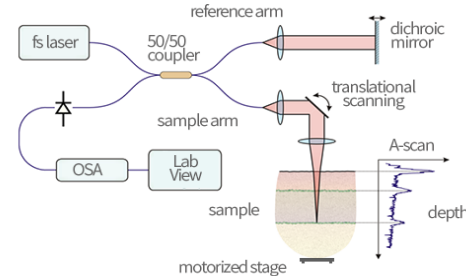


Figure 1. Schematic diagram of proposed imaging modality used to extract volumetric information from backscattered 1550nm laser source.

III. RESULTS & DISCUSSION

Before applying DFT technology, the Optical Spectrum Analyzer (OSA) captured raw spectral encoding from the laser source, with a travel delay of 7.7 uW between sample and reference arm power (Fig. 2).

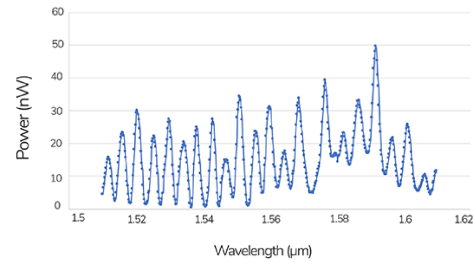


Figure 2. Signals backscattered from different depths and amplified at varying optical frequencies.

A Fast-Fourier transformation was applied to the raw spectral encoding in the frequency domain to extract the resolution capabilities of the imaging system in the time domain (Fig. 3).



Figure 3: High-speed, in vivo volumetric imaging is made possible by applying a series of concepts including depth-encoded frequency conversion ($L \rightarrow \omega$) and optical DFT ($\omega \rightarrow T$).

After taking a FWHM, the Fourier-transformed signal yielded a 2.24ps time, corresponding to an axial resolution of 8 microns, well within the preferred range of 5 to 10 μ m. As for translational imaging quality, the 1.50ps FWHM produced a transverse resolution of 4.9 microns at the higher end of the 3 to 5 μ m spectrum.

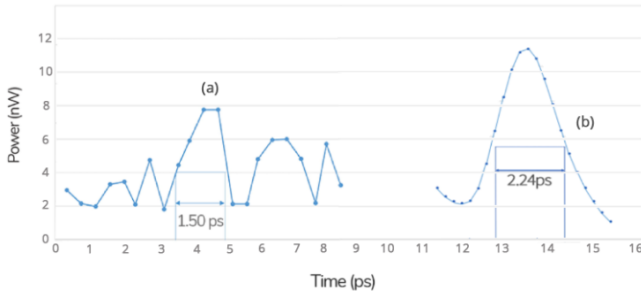


Figure 4. Translational, XY-plane (a), and axial, Z-plane (b), imaging resolution in the time domain extracted from the depth-encoded signal.

High contrast interference patterns were successfully created, using only a CUDA GPU workstation, FPGA-digitizer, and programs developed in Labview to automatically increment the movement of a motorized stage in the transverse axis.

The near-maximum axial and transverse imaging quality demonstrated by this study shows the versatility of rudimentary OCT systems in achieving spatial resolution within ± 2 microns of the preferred value. The use of FD-OCT opens numerous applications in the cross-sectional visualization of tissue morphologies.

While the results shown advance imaging speed and detection sensitivity capabilities, multi-photon microscopy (MPM), specifically three-photon microscopy (3PM), provides unsurpassed imaging depth into tissue by strongly suppressing the background signal and absorbing near-infrared excitation light. Future research will focus on incorporating unconventional optical illumination wavelengths in the 1700-1800 nm range to strike a balance between tissue scattering and water absorption.

IV. ACKNOWLEDGEMENTS

I would like to thank Dr. Shu-Wei Huang and Maxwell Adolphson with the Ultrafast Photonics Research Group at the University of Colorado, Boulder for their mentorship.

V. REFERENCES

- [1] J. G. Fujimoto, M. E. Brezinski, G. J. Tearney, et al., "Optical biopsy and imaging using optical coherence tomography", *Nature Med.* 1, 970 (1995).
- [2] T. Klein and R. Huber, "High-speed OCT light sources and systems [Invited]", *Biomed. Opt. Express* 8, 828 (2017).

Fluorescence Quenching by 4-(2-hydroxyethyl)-1-piperazineethanesulfonic

Riya Patel

Abstract – Quenching in fluorescence spectroscopy is crucial in numerous applications and can reveal important information about biochemical systems. The purpose of this study was to investigate if the 4-(2-hydroxyethyl)-1-piperazineethanesulfonic acid (HEPES) has a quenching effect and draw a correlation between reduction potential and quenching. Although for C343 the quenching effect was negligible, HEPES decreased the fluorescence responses of the BODIPY dyes significantly. A direct correlation between quenching rate and reduction potential was established.

I. INTRODUCTION

In fluorescence spectroscopy, fluorescence intensity of fluorophores dictate the applications and efficiency of fluorophores[1]. Quenching, any decrease in fluorescence intensity, can reveal information about biochemical systems and the electron transfers among donor-acceptor systems [2]. There are numerous applications of quenching: proteins, membranes, fluorescence probes research and indication of DNA hybridization and potassium ions and dye sensitized solar cells [3]. Quenching is quantitatively measured using the Stern-Volmer equation[4].

The reduction potential, or how easily a molecule can gain electrons, can help predict quenching rates in cases where quenching occurs due to electron transfer.

Anilines, piperidines, pyrazines, and morpholines, molecules that are similar to Good's buffers, have caused quenching among various fluorophores [5]. Good's buffers were developed during 1966–1980 specifically for biochemical and biological studies. A specific Good's buffer is 4-(2-hydroxyethyl)-1-piperazineethanesulfonic acid (HEPES) which is often used environmental, analytical and biological [6]. This paper will focus on how the HEPES buffer affects the fluorescence intensity of three different fluorophores.

The three fluorophores used in this study are Coumarin 343 Ethanolamine Amide Derivative (C343), BODIPY FL, and BODIPY FL-iso-chloride. The excitation and emission wavelengths and the electrochemical properties are included for each fluorophore in Table 1. C343 is often used in laser dyes, synthesizing electrodes and development of chemosensors and polymers [7]. BODIPY FL is used in the separation of glycosphingolipids, monitoring protein synthesis and in fluorescent probes [8]. BODIPY FL Iso-Chloride is a newly synthesized fluorophore and was used in this study to analyze its photophysical properties. These two commonly used classes of fluorophores have many wide applications and therefore were chosen to be studied.

Currently, it is unclear whether there is a quenching effect of fluorophores caused by buffers. The purpose of this study is to determine if the HEPES buffer has a quenching effect on three fluorophores, C343, BODIPY FL and BODIPY FL Iso-Chloride, and to draw a correlation between reduction potential and quenching.

II. METHODS

A 500 mM stock solution of HEPES was prepared from Sigma Life Science (Lot #SLBK 1535V). Dilutions ranging from 5mM to 400mM HEPES were created. 1M KOH and 1M HCl were used to adjust the pH to 8.00 ± 0.02 .

Three sets of titrations were done: each fluorophore with increasing concentrations of HEPES. The instruments used were an Agilent Technologies Carian Cary 100 UV-Vis Spectrophotometer and a QuantaMaster 40 Photon Technologies. To begin the titration, 1.5 mL of 0mM HEPES buffer was added into two cuvettes. One was placed in the reference slot and the other in the sample slot of the UV-Vis spectrophotometer. The sample cuvette was then removed and placed into the fluorimeter. The cuvette was rinsed three times with water and once with acetone. N₂ gas was used to dry the cuvette. This was repeated for all the remaining concentrations of HEPES and then for each fluorophore.

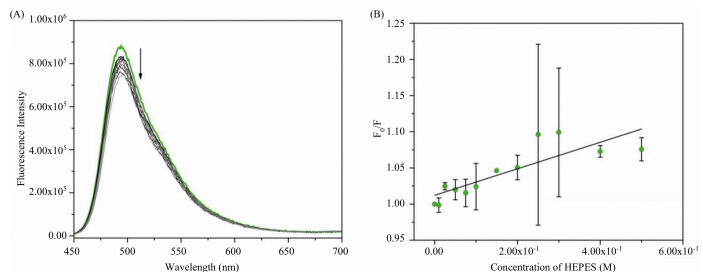


Figure 1. Emission Spectra from Quantamaster 40 Photon Technologies (A) and Stern-Volmer Plot (B) of C343 in presence of increasing concentration of HEPES buffer at 25 °C. Y-error bars in Figure 1B show standard deviation.

III. RESULTS AND DISCUSSION

Three titrations with various concentrations of the HEPES buffer and the three different fluorophores were performed to analyze the effect of the HEPES buffer on fluorescence intensity.

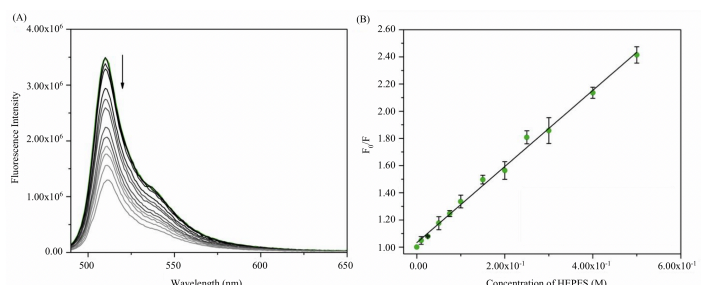


Figure 2. Emission Spectra from Quantamaster 40 Photon Technologies (A) and Stern-Volmer Plot (B) of C343 in presence of increasing concentration of HEPES buffer at 25 °C. Y-error bars in Figure 2B show standard deviation.

The emission spectra for the C343 titration shows minimum gaps between each trace and it seems as if the lines are on top of each other (Figure 2A). This indicates as

the concentrations of HEPES buffer increases, the fluorescence intensities do not change significantly, signifying the HEPES buffer does not have a quenching effect. The Stern-Volmer Plot shows a very small slope of 0.18301 indicating a negligible quenching rate (Figure 2B) [9]. (Table 1)

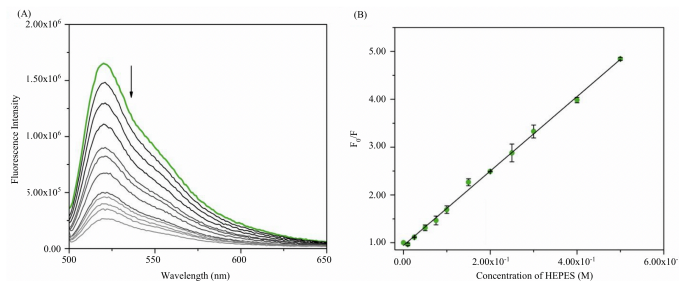


Figure 3. Emission Spectra from Quantamaster 40 Photon Technologies (A) and Stern-Volmer Plot (B) of BODIPY FL Iso-Chloride in presence of increasing concentration of HEPES buffer at 25 °C. Y-error bars in Figure 3B show standard deviation.

Properties	Fluorophore		
	C343	BODIPY FL	BODIPY FL Iso-Chloride
Excitation λ	446 nm	503 nm	500 nm
Emission λ	462 nm	512 nm	521 nm
Reduction Potential	-1.652V vs. SCE	-1.004V vs. SCE	-0.832V vs. SCE

Table 1.

In the emission spectra for BODIPY FL, there are larger gaps in the fluorescent intensity of the traces as concentrations of HEPES increase (Figure 3A). The Stern-Volmer Plot has a slope of 2.80248 (Figure 3B) [11].

The reduction potential of BODIPY FL is -1.004 V vs. SCE which is higher than C343 showing that more easily reduced fluorophores result in greater amounts of quenching (Table 1).

The emission spectra for the BODIPY FL-iso-chloride has very large gaps between each trace showing that as concentrations of the HEPES buffer increase, they have greater decreasing effects on fluorescence intensity (Figure 3A). The Stern-Volmer Plot shows the highest slope of 7.78364 for all three titrations (Figure 3B). BODIPY FL-Iso-Chloride had the highest reduction potential of -0.832 V vs. SCE—showing that it is easily reduced-- and also the greatest amount of quenching [10].

IV. RESULTS AND DISCUSSION

The effect of increasing concentrations of the HEPES buffer in presence of fluorophores with different electrochemical properties were studied. The fluorophores that are easily reduced showed higher quenching effect by the HEPES buffer. Therefore, it can be established that there is a direct correlation between the quenching by the HEPES buffer and reduction potential. Thus, fluorophores that are easily reduced (low reduction potentials) should always be investigated to see if a quencher can induce significant quenching. C343 had a negligible amount of quenching, however BODIPY FL and BODIPY FL-Iso Chloride had significant amounts of quenching. Although the HEPES is very commonly employed, it may not be a

good buffer for photophysical characterization of easily reduced fluorescent dyes because of its ability to quench fluorescence intensity.

Future investigations should include studying more aqueous buffers and fluorophores to determine if this correlation between reduction potential and quenching rate is consistent [3]. Other fluorophores that should be investigated include Alexa dyes, eFluor dyes, oxazaines, and Nile blue dyes[12]. In addition, using time resolved fluorescence spectroscopy and analyzing absorption spectra can reveal vital information about the mechanism of quenching which is crucial in determining its applications like in dye sensitized solar cells and fluorescent probes [13].

V. ACKNOWLEDGEMENTS

I would like to thank Claudia Yan for helping me along this research process.

VI. REFERENCES

- [1] L. Mátyus, J. Szöllősi, and A. Jenei, "Steady-state fluorescence quenching applications for studying protein structure and dynamics," *Journal of Photochemistry and Photobiology B: Biology*, vol. 83, no. 3, pp. 223–236, 2006.
- [2] J. R. Lakowicz, *Principles of Fluorescence Spectroscopy*. Boston, MA: Springer Science Business Media, LLC, 2006.
- [3] J. R. Lakowicz, *Topics in fluorescence spectroscopy*, vol. 2. New York: Plenum Press, 1992.
- [4] "Fluorescence Quenching." Zurich.
- [5] M. A. Jhonsi and A. Kathiravan, "Reductive fluorescence quenching of DMP with aniline," *Journal of Luminescence*, vol. 145, pp. 188–193, 2014.
- [6] C. M. H. Ferreira, I. S. S. Pinto, E. V. Soares, and H. M. V. M. Soares, "(Un)suitability of the use of pH buffers in biological, biochemical and environmental studies and their interaction with metal ions – a review," *RSC Advances*, vol. 5, no. 39, pp. 30989–31003, 2015.
- [7] X. Liu, H. Yin, H. Li, and Y. Shi, "Altering intra- to intermolecular hydrogen bonding by dimethylsulfoxide: A TDDFT study of charge transfer for C343," *Spectrochimica Acta Part A: Molecular and Biomolecular Spectroscopy*, vol. 177, pp. 1–5, 2017.
- [8] K. Perronet, P. Bouyer, N. Westbrook, N. Soler, D. Fourmy, and S. Yoshizawa, "Single molecule fluorescence detection of BODIPY-FL molecules for monitoring protein synthesis," *Journal of Luminescence*, vol. 127, no. 1, pp. 264–268, 2007.
- [9] O. Stern and M. Volmer, "Decay of Fluorescence," *Journal of the Röntgen Society*, vol. 15, no. 61, pp. 133–133, 1919.
- [10] A. Reule, "Errors in spectrophotometry and calibration procedures to avoid them," *Journal of Research of the National Bureau of Standards Section A: Physics and Chemistry*, vol. 80A, no. 4, p. 609, 1976.
- [11] C. A. M. Seidel, A. Schulz, and M. H. M. Sauer, "Nucleobase-Specific Quenching of Fluorescent Dyes. 1. Nucleobase One-Electron Redox Potentials and Their Correlation with Static and Dynamic Quenching Efficiencies," *The Journal of Physical Chemistry*, vol. 100, no. 13, pp. 5541–5553, 1996.
- [12] F. Preffer and D. Dombrowski, "Advances in complex multiparameter flow cytometry technology: Applications in stem cell research," *Cytometry Part B: Clinical Cytometry*, vol. 76B, no. 5, pp. 295–314, 2009.
- [13] H. Klifout, A. Stewart, M. Elkhalfia, H. He, "BODIPYs for Dye-Sensitized Solar Cells" *ACS Applied Materials & Interfaces*, vol. 9, no. 47, pp. 39873–39889, 2017.

Stabilization of Amorphous DDT in Polymers to Increase Lethality

Ethan Reiter

Abstract – Dichloro-diphenyl-trichloroethane (DDT) is a toxic contact insecticide used in disease-stricken regions for vector control, which is the management of disease-transmitting organisms' populations. This paper investigates the capacity of various polymers to stabilize DDT's amorphous state, its most lethal form to insects, and thereby increase its insecticidal efficacy. Improved stabilization of DDT's most lethal form would more effectively neutralize mosquitos, the arguably deadliest disease transmitters, therefore minimizing the DDT usage required for vector control.

I. INTRODUCTION

DDT neutralizes insects upon contact by opening neuronal Na^+ channels [1]. The resulting spontaneous neuronal firing eventuates in fatal spasms, empowering effective vector control in disease-stricken regions. Yet DDT's connections to environmental damage and chronic health conditions necessitate more lethal applications to minimize usage and thereby lessen vector control's environmental footprint.

Previous studies examining polymorphs of DDT [2] and lindane (γ -hexachloro-cyclohexane) [3] suggest that Ostwald's "Stage Rule," which inversely relates polymorphs' crystallization orders to their thermodynamic stabilities, may exist for polymorph lethality: more thermodynamically unstable forms can kill quicker. It is thus important to delay nucleation onset by stabilizing insecticides' amorphous (least stable) states. Such stabilization inhibits crystallization of less lethal forms, ultimately increasing lethality and reducing insecticide usage.

II. METHODS

The polymers polyethylene glycol (PEG), polyvinylpyrrolidone (PVP), polystyrene (PS), polymethyl methacrylate (PMMA), and polyvinyl acetate (PVAc) were individually combined with DDT at varying weight ratios and dissolved in chloroform, which was chosen for its ability to quickly dissolve all above polymers. Solutions were coated on glass slides at 1000 rpm for 2 sec, and then 2000 rpm for 20 sec using a SCS 6800 Spin Coating system, preceding drying at 25°C. Nucleation time was observed through a microscope fitted with crossed polarizers (Olympus BX50) and equipped with a digital camera; a hot stage (Mettler FP82HT) was used for temperature control at 25°C.

III. RESULTS AND DISCUSSION

Both polymer type and polymer-DDT weight ratios (W/Rs) greatly affected the nucleation rate of DDT at 25°C. For PEG(200 kDA)-DDT (2:1 W/R) films, DDT crystals developed after 10 min. Varying molecular weights of PEG over a range of 6 kDA to 200 kDA failed to affect crystallization. Nucleation time increased to 12 hrs with PVP-DDT (2:1 W/R) films. Moreover, increased polymer-DDT W/Rs seemingly inhibited nucleation;

PVP-DDT (10:1 W/R) films stabilized amorphous DDT for 40 hrs.

Polystyrene exhibited similar results. Nucleation onset time for PS(250 kDA)-DDT films increased from 24 hrs (1:2 W/R) to 6 days (1:1 W/R), and then to 45 days (2:1 W/R) as W/R increased. PMMA(350 kDA)-DDT and PVAc-DDT films likewise stabilized amorphous DDT for 45 days (2:1 W/R), at which point 10 μm -sized DDT crystals began to form. Overall, DDT-polymer films enabled prolonged stabilization of DDT's most lethal amorphous form through inhibiting nucleation of other solid-state forms.

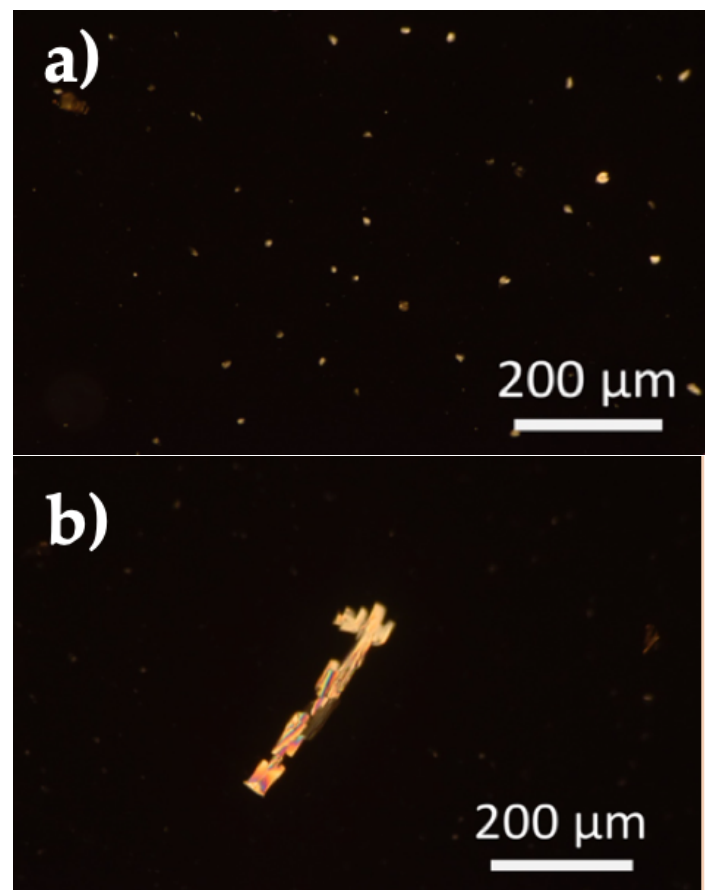


Figure 1: (a) PS(250 kDA)-DDT film (1:1 W/R), 6-day nucleation onset, and (b) PVAc-DDT film (1:2 W/R), 45-day nucleation onset, are juxtaposed. The inverse relationship between polymer-film W/R and DDT crystallization is visualized [4].

IV. CONCLUSION

Mosquitos, responsible for malaria, Zika virus, dengue fever, and yellow fever outbreaks, will only become more dangerous as global warming expands the scope of their habitats. Alleviating public health concerns requires more effective mosquito vector control, making the development of efficacious yet minimally toxic insecticides an imperative. Fortunately, the stabilization of existing insecticides in their most lethal chemical states empowers the fruition of public health goals while concurrently minimizing environmental damage—a long-desired equilibrium.

Moreover, though DDT was chosen as a model compound, polymer-film stabilization may lend itself to future research with other widespread insecticides such as dicofol and lindane. Its ability to integrate common polymers and insecticide also introduces the possibility of more effective insecticidal mosquito netting for enhanced vector control. Additionally, future research can evaluate other polymers like polyethylene terephthalate (PET) and nylon, polymers of different molecular weights, and cross-linked polymers.

IV. ACKNOWLEDGMENTS

I sincerely thank Dr. Jingxiang Yang and Dr. Bart Kahr for graciously providing necessary materials, facilities, and unwavering support. Research supported by New York University, the U.S. NSF (DMR-1105000, DMR-1608374), and the MRSEC program of the NSF under Award No. DMR-1420073. I also owe gratitude to Dr. Starace, Mr. Kuziola, and Mrs. Kaspriskie of Livingston High School's science research program for their obliging support.

V. REFERENCES

- [1] Davies, T. G. E., et al. "DDT, Pyrethrins, Pyrethroids and Insect Sodium Channels." *IUBMB Life*, vol. 59, no. 3, 3 Jan. 2008, pp. 151–162., doi:10.1080/15216540701352042.
- [2] Yang, Jingxiang, et al. "DDT Polymorphism and the Lethality of Crystal Forms." *Angewandte Chemie*, vol. 56, no. 34, 14 Aug. 2017, pp. 10165–10169., doi:10.1002/ange.201703028.
- [3] Yang, Jingxiang, et al. Rule of Stages for Insecticide Polymorph Lethality. New York University, 2018.
- [4] Unpublished work from Dr. Bart Kahr's group, 2018

QuitPuff: A Simple, Home-based, Salivary Diagnostic Test to assess Risk of Oral Pre-cancer and Cancer in Chronic Smokers

Nikhiya Shamsher

Abstract - High mortality rate in oral cancer is mainly due to late diagnosis. Current methods involve complex laboratory procedures and are unavailable in rural areas. In this study, a simple, home-based salivary diagnostic test for smokers is devised for early detection of oral pre-cancer and cancer.

I. INTRODUCTION

Oral cancer is a cancerous growth in the oral cavity [1]. It most commonly involves the tongue, floor of the mouth, cheek lining, gums, lips or roof of the mouth. More than 90% of all oral cancers are squamous cell carcinoma [2].

In India, the incidence of oral cancer is the highest, accounting for almost one third cases found in the world [1]. The high prevalence is mainly due to influence of tobacco and betel quid chewing [4]. Over 5 people in India die every hour every day because of oral cancer [3]. The high mortality rate is attributed mainly to late diagnosis either due to ignorance or inaccessibility of medical care [1,2,7]. Most patients seek help only in the late stages when the symptoms are more prominent [1]. Detection of an oral cancer at stage I carries a prognosis of 80% survival, while the same lesion at stage III carries a 20% survival [8]. This difference could affect not only the quality of life for the patients but also the treatment cost. Thus, there is a need for improvement in early risk detection of oral carcinomas because in the initial stages treatment is more effective and morbidity is minimal.

Exposure to cigarette smoke/ tobacco is responsible for 90% cases of oral cancer [14]. When people smoke they generate Reactive Oxygen Species (ROS). ROS induced cell damage causes lipid peroxidation which is implicated in the pathogenesis of oral cancer [9,10,11,14,15]. It most commonly affects the polyunsaturated fatty acids, causing alteration in the structure and function of cell membranes. Cancer development is caused by cumulative action of multiple events i.e. initiation, promotion and progression, occurring in a single cell. ROS not only initiates but also promotes this multistep carcinogenesis [10]. Malondialdehyde (MDA) is the end product of lipid peroxidation and can be used as a marker for assessing the degree of lipid peroxidation [9,10,11,14,15]. MDA is mutagenic, genotoxic and a potential carcinogen and readily reacts with deoxy nucleosides to produce adducts causing DNA damage [11]. An increase in salivary MDA is widely reported in various oral pre-cancers & cancers in the early stages [9,10,11,12, 13,14,15].

II. METHOD

One molecule of Malondialdehyde (MDA) reacts with two molecules of Thiobarbituric Acid (TBA) in an acidic medium at high temperature to produce a coloured adduct. A highly sensitive Thiobarbituric Acid (TBA) reagent was formulated by dissolving 0.375g of TBA in 85% Ortho-Phosphoric acid (1ml) and 1% Trichloro-Acetic Acid (1ml). MDA standards in saliva of 10 healthy people were prepared in the concentrations of 500, 250, 100, 50, 25 and 5ng/ml and TBA reaction was performed. The color change was noted.

Samples were analysed by UV Spectroscopy, absorbance measured at 532nm, a standard curve (Figure 1) and colorimetric chart (Figure 2) were prepared.

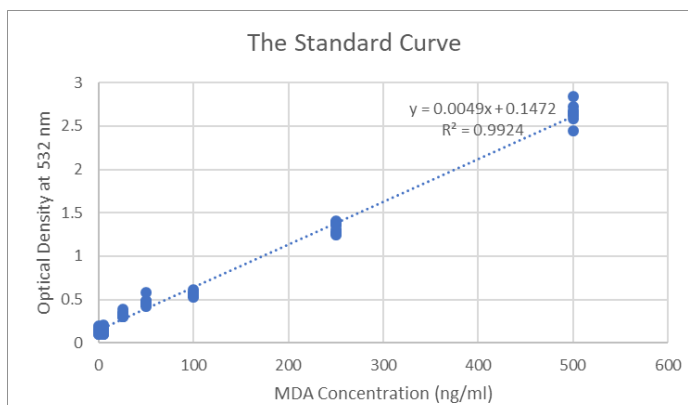


Figure 1: The Standard Curve

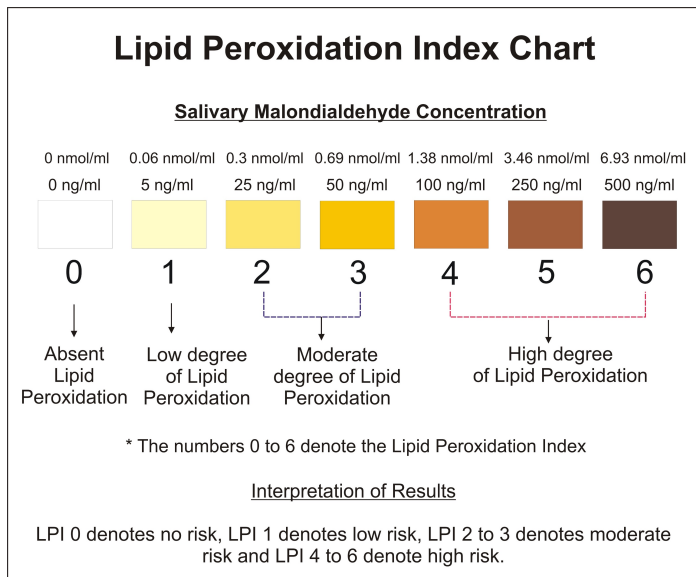


Figure 2: The Colorimetric Lipid Peroxidation Index Chart

The method was tested on 125 people (5 groups) from BMCRI Hospital. Ethics approval was granted by IEC. Informed consent was obtained. Group 1 had 25 non-smokers, Group 2, 3 and 4 consisted of 25 smokers who smoked less than 10, between 10-20 and more than 20 cigarettes per day respectively, none of them had any oral lesions, Group 5 consisted of 25 smokers who smoked 10-20 cigarettes a day, 20 with recently diagnosed pre-cancerous mouth lesions and 5 with Oral Squamous Cell Carcinoma stage 1-2, yet to start on treatment. Tests were done on fresh saliva samples. 1ml of saliva was taken in a test tube, 2ml of TBA Reagent was added and the mixture was heated in a boiling water bath for 15 minutes. The color change was matched with the colorimetric chart and the Lipid Peroxidation Index (LPI) was

noted. The test method was validated for its performance using the standard curve. All 125 samples were analyzed by UV Spectroscopy and the standard curve equation was used to determine the MDA levels. Based on the MDA values obtained by the validation method, the LPI (Lipid Peroxidation Index) was again derived and noted.

III. RESULTS AND CONCLUSION

The mean Lipid Peroxidation Index (LPI) obtained by the test method was compared with the mean LPI obtained by the validation method. The results agreed (Table 1). Two types of variations were found, small in 12% cases & large in 3.2% cases. Small variations were defined as those where a minor difference was found between the LPIs from the test and validation method. These minor variations did not warrant a zone change (low, moderate, high) in the LPI chart and hence considered as small variations. Large variations were defined as those where a large difference was found between the LPIs from the test and validation method, warranting a zone change. For purposes of calculation of accuracy only large variations were taken into consideration and thus it is derived that the diagnostic test was able to detect the degree of salivary lipid peroxidation with 96.8% accuracy.

Smokers exhibited a higher degree of salivary lipid peroxidation as compared to non-smokers, heavier the smoker, higher was the degree of lipid peroxidation (Table 2).

Table 1: Comparison between the mean LPIs (Lipid Peroxidation Index) obtained by test and validation method.

Group Name	Mean LPI obtained by test method	Mean LPI by validation method
Group 1	0.2	0.24
Group 2	3.64	3.56
Group 3	3.68	3.64
Group 4	4.52	4.48
Group 5	4.48	4.32

Table 2: Degree of Lipid Peroxidation in Study Groups

Group Name	Total No	Degree of	Lipid	Peroxidation
		Zero	Low	Moderate
Group1	25	20	4	1
Group2	25	0	0	9
Group3	25	1	0	6
Group4	25	0	0	3
Group5	25	0	0	1
				High
				0
				16
				18
				22
				24

QuitPuff, a simple, quick, home-based, inexpensive method can serve as an early, non-invasive test for smokers to assess risk of oral pre-cancer & cancer.

IV. ACKNOWLEDGEMENT

I thank Chaithanya P, Dr. Tania Das, Madhavi L, Dr. Muralidhan, and Dr. Arnab Roy for mentoring me.

V. REFERENCES

- [1] Bano S, "Salivary biomarkers for oral squamous cell carcinoma: An overview." IJSS Case Reports & Reviews 2015, 1(8), 39-45.
- [2] Markopoulos AK, "Salivary Markers for Oral Cancer Detection." Open Dent J., 2010, 4, 172-8.
- [3] Gupta B, "Oral cancer in India continues in epidemic proportions: Evidence base and policy initiatives." International Dental Journal 2013, Feb 63(1), 12-25.
- [4] Liviu Feller, "Oral Squamous Cell Carcinoma: Epidemiology, Clinical Presentation and Treatment." Journal of Cancer Therapy 2012, 3(4), 263-8.
- [5] Krishna Rao SV, "Epidemiology of Oral Cancer in Asia in the Past Decade- An Update (2000-2012)." Asian Pacific Journal of Cancer Prevention 2013, 14(10), 5567-77
- [6] Lin WJ, "Smoking, Alcohol, and Betel Quid and Oral Cancer: A Prospective Cohort Study." Journal of Oncology 2011, Article ID 525976, 5 pages.
- [7] Mehrotra R, "Oral squamous cell carcinoma: Etiology, pathogenesis and prognostic value of genomic alterations." Indian J Cancer 2006, 43(2), 60-6.
- [8] Shah FD, "A Review on Salivary Genomics and Proteomics Biomarkers in Oral Cancer." Ind J Clin Biochem. 2011, 26(4), 326-334.
- [9] Shetty SR, "Status of salivary lipid peroxidation in oral cancer and precancer." Indian Journal of Medical and Paediatric Oncology: Official Journal of Indian Society of Medical & Paediatric Oncology. 2014, 35(2), 156-8.
- [10] Rai B, "Salivary Lipid Peroxidation Product Malonaldehyde in Various Dental Diseases." World Journal of Medical Sciences 2006, 1(2), 100-101.
- [11] Ganesan A, "Assessment of Lipid Peroxides in Multiple Biofluids of Leukoplakia and Oral Squamous Cell Carcinoma Patients- A Clinico- Biochemical Study." Journal of Clinical and Diagnostic Research 2014, 8(8), ZC55-ZC58.
- [12] Abdolsamadi H, "Levels of salivary antioxidant vitamins and lipid peroxidation in patients with oral lichen planus and healthy individuals." Chonnam Med J. 2014, 50, 58-62.
- [13] Kaur J, "Salivary 8-hydroxy-2-deoxyguanosine, malondialdehyde, vitamin C, and vitamin E in oral pre-cancer and cancer: diagnostic value and free radical mechanism of action." Clin Oral Invest. 2016, 20, 315-9.
- [14] Arathi A, "Salivary malondialdehyde and antioxidant status in oral squamous cell carcinoma patients and smokers." Biomedical Research. 2010, 21(1), 67-70.
- [15] Shivashankara AR, "Salivary Total Protein, Sialic Acid, Lipid Peroxidation and Glutathione in Oral Squamous Cell Carcinoma." Biomedical Research. 2011, 22 (3), 355-359.



Columbia Undergraduate Science Journal

The *Columbia Junior Science Journal* (CJSJ) is an extension of the *Columbia Undergraduate Science Journal* (CUSJ), an open-access science journal that is committed to publishing undergraduate manuscripts of the highest scholarship resulting from significant scientific research or outstanding scientific analysis. The CJSJ provides high school students with a platform to publish manuscripts in the fields of natural sciences, physical sciences, engineering, and social sciences.